The Astrophysical Journal, 905:133 (23pp), 2020 December 20 https://doi.org/10.3847/1538-4357/abc875

Characterizing the Circumgalactic Medium of the Lowest-mass Galaxies: A Case Study of IC 1613

Yong Zheng[1,2], Andrew Emerick[3,4,9], Mary E. Putman[5], Jessica K. Werk[6], Evan N. Kirby[7], and Joshua Peek[8]
[1] Department of Astronomy, University of California, Berkeley, CA 94720, USA; yongzheng@berkeley.edu
[2] Miller Institute for Basic Research in Science, University of California, Berkeley, CA 94720, USA
[3] Carnegie Observatories, Pasadena, CA, 91101, USA
[4] TAPIR, California Institute of Technology, Pasadena, CA, 91125, USA
[5] Department of Astronomy, Columbia University, New York, NY 10027, USA
[6] Department of Astronomy, University of Washington, Seattle, WA 98195, USA
[7] Astronomy Department, California Institute of Technology, Pasadena, CA 91125, USA
[8] Space Telescope Science Institute, 3700 San Martin Drive, Baltimore, MD 21218, USA
Received 2020 August 11; revised 2020 October 26; accepted 2020 November 6; published 2020 December 22

Abstract

Using 10 sight lines observed with the Hubble Space Telescope/Cosmic Origins Spectrograph, we study the circumgalactic medium (CGM) and outflows of IC 1613, which is a low-mass ($M_* \sim 10^8\,M_\odot$), dwarf irregular galaxy on the outskirts of the Local Group. Among the sight lines, four are pointed toward UV-bright stars in IC 1613, and the other six sight lines are background QSOs at impact parameters from 6 kpc ($<0.1R_{200}$) to 61 kpc ($0.6R_{200}$). We detect a number of Si II, Si III, Si IV, C II, and C IV absorbers, most of which have velocities less than the escape velocity of IC 1613 and thus are gravitationally bound. The line strengths of these ion absorbers are consistent with the CGM absorbers detected in dwarf galaxies at low redshifts. Assuming that Si II, Si III, and Si IV comprise nearly 100% of the total silicon, we find 3% ($\sim 8 \times 10^3\,M_\odot$), 2% ($\sim 7 \times 10^3\,M_\odot$), and 32%–42% [$\sim$(1.0–1.3) $\times\ 10^5\,M_\odot$] of the silicon mass in the stars, interstellar medium, and within $0.6R_{200}$ of the CGM of IC 1613. We also estimate the metal outflow rate to be $\dot{M}_{\rm out,Z} \geqslant 1.1 \times 10^{-5}\,M_\odot\,{\rm yr}^{-1}$ and the instantaneous metal mass loading factor to be $\eta_Z \geqslant 0.004$, which are in broad agreement with available observation and simulation values. This work is the first time a dwarf galaxy of such low mass is probed by a number of both QSO and stellar sight lines, and it shows that the CGM of low-mass, gas-rich galaxies can be a large reservoir enriched with metals from past and ongoing outflows.

Unified Astronomy Thesaurus concepts: Circumgalactic medium (1879); Local Group (929); Magellanic Stream (991); Metallicity (1031); Dwarf irregular galaxies (417)

1. Introduction

Galaxies at redshift $\lesssim$2.5 have lost the majority of the metals produced over their star formation histories, giving rise to the so-called missing metals problem (e.g., Bouché et al. 2007; Peeples et al. 2014). For instance, Peeples et al. (2014) show that local star-forming galaxies with stellar masses $M_* = 10^{9.3}$–$10^{11.6}\,M_\odot$ only contain 20%–25% of metals in their stars and interstellar medium (ISM). Detailed studies of single galaxies yield similar results. For example, Telford et al. (2019) find that 62% of the metal mass formed within $r < 19$ kpc is missing from M31's disk based on resolved star formation history analyses with data from the Panchromatic Hubble Andromeda Treasury (Dalcanton et al. 2012). The missing metals problem is found to be the most severe in low-mass dwarf galaxies, which contain fewer metals than their higher-mass counterparts according to the gas-phase (Tremonti et al. 2004; Lee et al. 2006; Andrews & Martini 2013) and stellar (Gallazzi et al. 2005; Kirby et al. 2013) mass–metallicity relations. In the Local Group (LG), dwarf galaxies are found to have lost $\gtrsim$96% of the iron they have synthesized through star formation (Kirby et al. 2011, 2013), with the missing iron located either in their ISM or CGM, and with some fraction possibly having escaped the galaxies altogether. While processes such as metal-poor gas infall or low star formation efficiency could contribute to the low metal abundances (e.g., Brooks et al. 2007; Calura et al. 2009), low-mass dwarf galaxies are prone to lose more metals via outflows due to their shallow gravitational potential (e.g., Mac Low & Ferrara 1999; Ma et al. 2016; Muratov et al. 2017; Christensen et al. 2018; Emerick et al. 2018; Romano et al. 2019).

It remains to be seen if the rest of the metals, if not in the main bodies of the galaxies, are within their circumgalactic medium (CGM) or have been ejected into the intergalactic medium (IGM). Cosmological and idealized hydrodynamic simulations have widely explored the metal content in dwarf and higher-mass galaxies (e.g., Brooks et al. 2007; Vogelsberger et al. 2014; Ma et al. 2016); however, only a few have focused on the distribution of metals in the CGM of low-mass dwarf galaxies with $M_* \lesssim 10^{8.5}\,M_\odot$ (Muratov et al. 2017; Christensen et al. 2018; Hafen et al. 2019). For example, Muratov et al. (2017) show that the metal content in a galaxy's CGM closely follows the star formation and outflow activities; for a dwarf galaxy with $M_* \sim 10^{8.5}\,M_\odot$, the CGM has gained most of its current metal mass ($10^{6.7}\,M_\odot$) since $z = 1$, and at $z = 0$, the metals in the CGM account for $\sim$40% of the total metal mass. Similarly, Christensen et al. (2018) show that for galaxies with $M_* \lesssim 10^{8.5}\,M_\odot$, less than 10% of the metals are retained in stars, $\sim$10%–30% of the metals are in the ISM, and the rest

[9] Carnegie Fellow in Theoretical Astrophysics.

Table 1
IC 1613 Information

Variable	Value	References
R.A.	$01^h04^m54^s.2$ (16.°2258)	1
DEC	$+02^d08^m00^s$ (2.°1333)	1
$D_\odot$	755 ± 42 kpc	2, 3
v_{helio}	-232 km s^{-1}	2, 4
v_{LSR}	-236 km s^{-1}	...
M_{HI}	$6.5 \times 10^7\ M_\odot$	2, 4, 5
σ_{HI}	25.0 ± 3.0 km s^{-1}	2, 4
12+log(O/H)	7.73 ± 0.04	6
M_*	$10^8\ M_\odot$	7
M_h	$4 \times 10^{10}\ M_\odot$	8
R_{200}	107 kpc	9
SFR	0.0025 $M_\odot$ yr^{-1}	10
θ	37.°9	11

Note. (1) Simbad. (2) McConnachie (2012). (3) Bernard et al. (2010). (4) Lake & Skillman (1989). (5) Silich et al. (2006). (6) Bresolin et al. (2007), from H II regions. (7) McConnachie (2012), stellar mass, assuming a stellar mass to light ratio of 1. (8) Dark-matter halo mass, converted from M_* based on the M_*–M_h relation from Moster et al. (2010). (9) Virial radius, defined with respect to 200 times the matter density $\rho_m \equiv \rho_c\Omega_m$. (10) Hunter & Elmegreen (2004). (11) Inclination angle determined from H I observation using VLA (Hunter et al. 2012).

are either in the CGM of the galaxies or have escaped beyond the virial radii.

Observationally, the quest to find baryons in dwarf galaxies' CGM has been limited to a few low-mass members in the LG (e.g., Bowen et al. 1997; Richter et al. 2017; Zheng et al. 2019b) and at low redshift (Bordoloi et al. 2014; Liang & Chen 2014; Johnson et al. 2017). For instance, Bordoloi et al. (2014) find a large reservoir of carbon with mass of $\geqslant 1.2 \times 10^6\ M_\odot$ in the CGM of 43 low-mass galaxies ($M_* \sim 10^{8.2}$–$10^{10.2}\ M_\odot$) at redshift $\leqslant 0.1$. Most of their C IV detection occur within 0.5 virial radius, beyond which no C IV is detected at a sensitivity limit of 50–100 mÅ. In the LG, Zheng et al. (2019b) find a total mass of $(0.2\text{–}1.0) \times 10^5\ M_\odot$ detected in Si II, Si III, and Si IV in the CGM of the dwarf galaxy Wolf–Lundmark–Melotte (WLM). Their detection is deemed tentative given the uncertain contamination from the Magellanic Stream in the foreground. In this work, we will address the Magellanic contamination in the context of the CGM absorbers of gas-rich galaxies, including IC 1613, in the LG.

IC 1613 is a dwarf irregular galaxy on the outskirts of the LG. With four stellar sight lines in the galaxy and six QSO sight lines in its halo observed with HST/COS, we seek to understand (1) how the metals are distributed in the stars, ISM, and CGM of IC 1613, and (2) how the metals travel to the CGM and what the instantaneous metal mass loading factor is. At $M_* = 10^8\ M_\odot$ (see Table 1), IC 1613 is among the lowest-mass galaxies to have been studied in the context of the CGM metal content and outflows. And with 10 sight lines at $<0.6R_{200}$ (see Figure 1), it is one of the rare cases where the CGM is probed by numerous QSO sight lines, with the exception of the Milky Way (e.g., Putman et al. 2012; Richter et al. 2017; Zheng et al. 2019a) and M31 (Howk et al. 2017; Lehner et al. 2020).

IC 1613 is an excellent candidate to study the CGM and metal flows for a number of reasons. First, it is isolated from other galaxies in the LG, with the nearest neighbor (M33) 400 kpc away (Hunter & Elmegreen 2004). Therefore, the galaxy's halo does not overlap with other halos. Second, IC 1613 is on the outskirts of the LG, in which case the gas in the galaxy has not been stripped off due to ram pressure and the galaxy's CGM is most likely to remain intact. Other galaxies that are close to the Milky Way or M31 have been found with their gas content largely stripped (Grcevich & Putman 2009; M. Putman et al. 2020, in preparation). Lastly, the galaxy has had a continuous and nearly constant star formation rate over the past >10 Gyr (Cole et al. 1999; Skillman et al. 2003, 2014; Weisz et al. 2014), which is conducive to a metal-enriched CGM and the presence of current outflows.

This paper is structured as follows: in Section 2, we elaborate on the data reduction, including spectral coaddition, continuum normalization, Voigt-profile fitting, line measurements, and auxiliary H I data sets. In Section 3, we study the connection between the detected absorbers and IC 1613, and in Section 4 we discuss the presence of the Magellanic Stream in the foreground. In Section 5, we estimate the metal budget of IC 1613 and the outflow's instantaneous metal mass loading factor and compare the results to predicted values from simulations. In Section 6, we compare our results with those of other dwarf galaxies at low redshifts and in the LG. We conclude in Section 7.

2. Data and Measurements

In Table 1, we summarize IC 1613's key properties that are used throughout this paper. The halo mass of IC 1613, $M_h = 4 \times 10^{10}\ M_\odot$, is estimated from M_* using the M_*–M_h relation from Moster et al. (2010). Note that at $M_* = 10^8\ M_\odot$, the M_*–M_h relation is highly uncertain. Our derived mass is consistent with the allowed M_h range derived for low-mass galaxies ($M_* < 10^8\ M_\odot$; Garrison-Kimmel et al. 2014, 2017). We arbitrarily define the boundary between the CGM and IGM as the galaxy's virial radius. Following the definition used by COS-Halos (Werk et al. 2013) and COS-Dwarfs (Bordoloi et al. 2014), we calculate the virial radius of IC 1613 as $R_{200} = (3/4\pi \mathrm{M_{halo}}/200\rho_\mathrm{m})^{1/3} = 107$ kpc, where $\rho_\mathrm{m} = \rho_\mathrm{c}\Omega_\mathrm{m}$ is the cosmic critical matter density at $z = 0$. Moreover, when examining the gas kinematics, we only consider CGM gas to be those absorbers with velocity less than the escape velocity of IC 1613 at the corresponding impact parameter (see Section 3).

Our data set includes six QSO sight lines (Q1–Q6) within the virial radius ($R_{200} = 107$ kpc or $\sim 8°$ at $d_\odot = 755$ kpc) of IC 1613 and four UV-bright OB star sight lines (S1–S4) in the galaxy itself, as shown in Figure 1 and Table 2. Among them, Q1, Q2, Q3, S1, and S2 (red dots in Figure 1) were observed with HST/COS program GO 15156. Because of a delayed guide-star acquisition failure, one of the HST visits for S2 that occurred on 2018 November 25 did not yield usable data. We filed a Hubble Observation Problem Report (HOPR 91429) and reobserved S2 for one more visit on 2018 Decmber 24. Our following analysis of S2 includes data from the new visit and the usable spectra from the original observation. We process all of the QSO and star spectra consistently as outlined below.

The rest of the targets were retrieved from the STScI/MAST archive observed by previous programs, including GO 12867 (S3, S4), 12275 (Q4), and 11585 (Q5, Q6). The archival target list was decided on 2019 July when our last search for publicly available sight lines occurred. In addition to the adopted sight lines, we found a few other QSO spectra near IC 1613 but

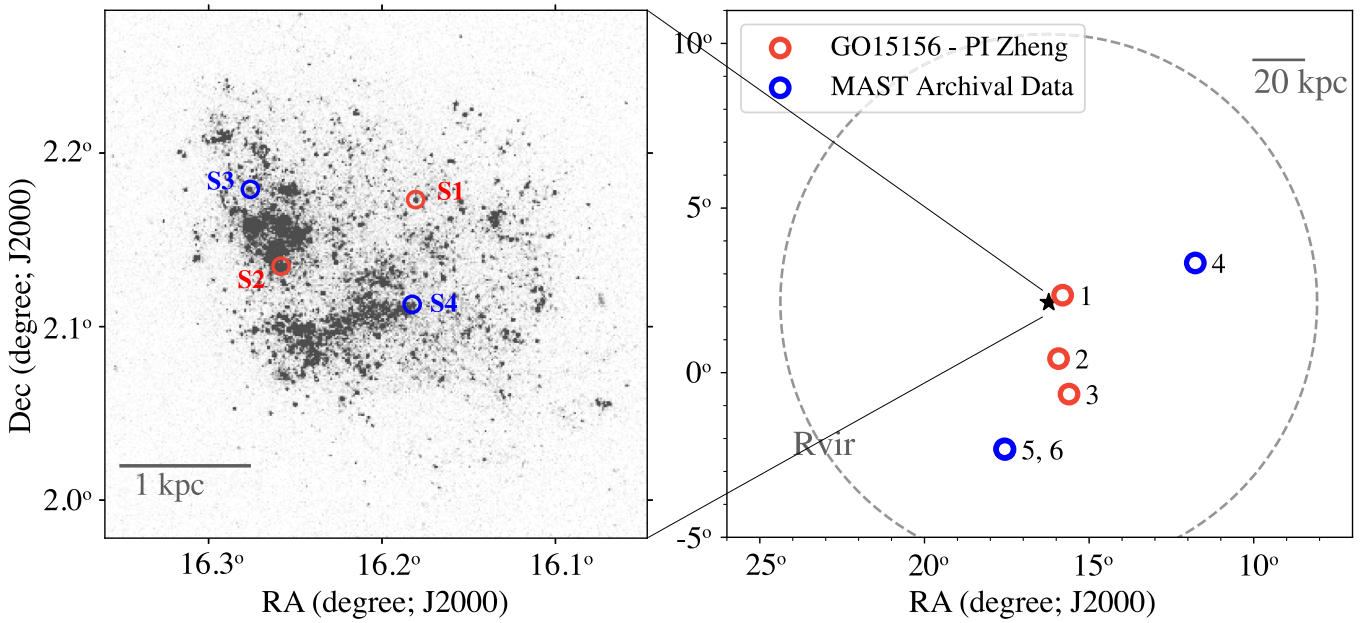

Figure 1. Left: we show the locations of the four UV-bright stars in IC 1613 against a far-UV background image from the GALEX Ultraviolet Atlas of Nearby Galaxies (Gil de Paz et al. 2007). Right: distribution of the six QSO sight lines within R_{200} of IC 1613 . Circles in red are new data observed with GO15156 (PI Zheng), and those in blue were retrieved from the STScI/MAST archive observed by previous programs (see Table 2).

Table 2
Target Information

Star ID	Target Name	R.A. (J2000) (degree)	Decl. (J2000) (degree)	v_{HI}[a] (km s^{-1})	S/N[b]	Spec. Type[c]	PI, Program[d]
S1	IC1613-C10	16.1806	+2.1732	−239.4	12.5	B1.5Ib	Zheng, 15156
S2	IC1613-B7[e]	16.2581	+2.1351	−234.3	15.2	O9I	Zheng, 15156
S3	IC1613-A13	16.2759	+2.1791	−231.7	11.8	O3?O4v((f))	Lanz, 12867
S4	IC1613-B11	16.1826	+2.1128	−242.0	10.5	O9.5I	Lanz, 12867
QSO ID	Target name	R.A. (J2000) (degree)	Decl. (J2000) (degree)	z[f]	S/N[b]	$d_{IC\ 1613}$[g] (kpc)	Program[d]
Q1	LBQS-0100+0205	15.8041	2.3528	0.393	8.9	6.3	Zheng, 15156
Q2	LBQS-0101+0009	15.9281	0.4270	0.394	7.8	22.8	Zheng, 15156
Q3	2MASX J01022632-0039045	15.6097	−0.6513	0.296	8.6	37.6	Zheng, 15156
Q4	PG 0044+030	11.7746	3.3319	0.624	6.3	60.7	Wakker, 12275
Q5	HB89-0107-025-NED05	17.5677	−2.3142	0.956	11.7	61.2	Crighton, 11585
Q6	LBQS-0107-0235	17.5547	−2.3314	0.957	12.2	61.4	Crighton, 11585

Notes.
[a] The systemic velocity of the ISM gas along the line of sight, measured from H I 21 cm emission from the VLA data cube.
[b] Signal-to-noise ratio (S/N) per resolution element for coadded spectra. Six pixels are assumed per resolution element for both G130M and G160M gratings. For each target, the S/N value is averaged over eight absorption-line free locations at 1120, 1170, 1320, 1370, 1420, 1470, 1520, 1620 Å. At each location, the S/N over a 10 Å spectral window is calculated.
[c] Spectral types from Simbad for stellar sight lines.
[d] PI and Program ID for each sight line.
[e] This target was named as IC 1613-010502-020805 in proposal GO15156.
[f] Redshifts of the QSOs.
[g] Impact parameter, or transverse distance, between the target and IC 1613.

decided not to use them because of the low signal-to-noise ratio (S/N) of the spectra.

2.1. Spectral Coaddition

We focus on data coaddition products from two community coadding routines: HST Spectroscopic Legacy Archive (HSLA) V2 Release and coadd_x1d.pro (Danforth et al. 2010). We decided to use HSLA when available and otherwise use the coadded spectra processed by coadd_x1d.pro that combine spectra from multiple exposures weighted by exposure times. We show in Appendix A that these two methods yield consistent coadded flux levels and line profiles. The typical wavelength accuracy for the COS spectra is 15–20 km s^{-1} (COS Instrument Handbook). Because the COS spectra have been oversampled with a native pixel size of 2.5 km s^{-1}, after the coaddition, we bin the spectra by 3 pixels to improve the S/N by a factor of $\sqrt{3}$.

2.2. Continuum Normalization, Voigt-profile Fitting, and Apparent Optical Depth Method

We measure transitions of ionized metal species that are commonly observed in a galaxy's CGM, including Si II 1190/1193/1260/1526 Å, Si III 1206 Å, Si IV 1393/1402 Å, C II 1334 Å, and C IV 1548/1550 Å. We also detect P II 1152 Å, S II 1250/1253/1259 Å, Fe II 1144/1608 Å, and Al II 1670 Å lines from sight lines S1–S4 but do not use these lines because they are typically related to a galaxy's ISM. Furthermore, we do not use C II* 1335 Å because the IC 1613's component of this line is always blended with the C II 1334 Å line from the Milky Way. The O I 1302 Å and Si II 1304 Å lines are not studied in this work due to the influence of the air-glow emission near 1302 Å from O I in the Earth's exosphere.

For continuum and Voigt-profile fitting, we used an IDL package developed for the COS-Halos survey as detailed in Tumlinson et al. (2013). We briefly summarize the major procedures as follows. First, for each line, the continuum normalization is done over a spectral window of $\pm 1000\,\mathrm{km\,s^{-1}}$ from its rest wavelength. Over this window, we manually mask any visible absorption features and fit the rest with Legendre polynomials at low orders and determine the best continuum fit by minimizing the reduced χ^2. We then proceed to conduct Voigt-profile fitting using the MPFIT package (Markwardt 2009). For ions with multiple transition lines, the Voigt-profile fitting is run simultaneously among all the lines to ensure consistent fits. We also use reduced-χ^2 minimization to evaluate the best-fit parameters, including column density ($\log N$), centroid velocity (v) in the rest frame of IC 1613, and Doppler width (b). The best-fit parameters are recorded in Table 3, and the relevant measurements are noted as "VP" in column (2). For each absorber, we also calculate its equivalent width (W_r) over a similar velocity range to the Voigt-profile fit result. We show the line profiles and fitting results in Figure 2 and Figures A3–A12 in Appendix A.

For absorbers that do not have robust Voigt-profile fits, we calculate their column densities ($\log N_\mathrm{AOD}$) using the apparent optical depth method (AOD; see Equation (6) in Savage & Sembach 1996). The AOD method is valid, with a requirement that the absorption line has to be resolved and unsaturated (Savage & Sembach 1991), which is not a problem here because the detection is weak among most sight lines. For the Si IV 1393/1402 and C IV 1548/1550 doublets, we adopt results from the stronger line (1393 and 1548). For Si II, because in many cases Si II 1260 is blended with S II 1259 from the Milky Way, we use the line measurements from Si II 1193 instead. For each absorber, we decide the AOD velocity integration range based on visual inspection of the absorption-line profile. For lines with no detection at the systemic velocity of IC 1613, the velocity range is set to be $[-50, 50]\,\mathrm{km\,s^{-1}}$ from the systemic velocity, and we report 3σ upper limit values of $\log N_\mathrm{AOD}$.

For S1–S4, as shown in Figure 2, the Si IV line shows extended profiles. Because of line saturation, we are unable to find robust Voigt-profile fits, and it is impractical to calculate $\log N_\mathrm{AOD}$ over the total velocity range which includes the ISM absorption. Thus, we do not use Si IV detected in these stellar sight lines. A similar decision was applied to Si III in S1 and C IV in S1 and S2.

2.3. Auxiliary H I 21 cm Data Sets

Three H I 21 cm data sets are included to study the neutral gas in and around IC 1613 . We use the VLA observation from the Little THINGS survey (Hunter et al. 2012) to probe the dense, cold H I in the ISM of the galaxy. Furthermore, we use data cubes from the GALFA-H I survey (Peek et al. 2011, 2018) and HI4PI Collaboration et al. (2016) to probe more diffuse gas in the galaxy as well as along QSO sight lines in the halo.

The Little THINGS survey provides two data sets, one with "natural weighting" and the other with "robust weight." We adopt the natural weighting data cube because it has a larger beam and is better at bringing out the diffuse H I emission from the disk. The data cube is in $\mathrm{Jy\,beam^{-1}}$, which we convert to brightness temperature in Kelvin as $\mathrm{S(mJy\,beam^{-1})} = 1.65 \times 10^{-3} \delta_\alpha \delta_\beta T_B(K)$, where $\delta_\alpha = 13\farcs2$ and $\delta_\beta = 11\farcs0$ are the FWHM of the major and minor axes of the beam given in Table 3 in Hunter et al. (2012). The GALFA-H I survey provides data with angular resolution of $\delta\theta = 4'$, spectral resolution of $\delta v = 0.184\,\mathrm{km\,s^{-1}}$, and brightness temperature sensitivity of 140 mK per $\mathrm{km\,s^{-1}}$ velocity channel (1σ). The HI4PI survey provides lower angular and spectral resolutions ($\delta\theta = 16.2'$, $\delta v = 1.49\,\mathrm{km\,s^{-1}}$), but higher sensitivity ($\sim$53 mK per $\mathrm{km\,s^{-1}}$ at 1σ). The H I spectra from these data are shown in Figure 2 and Figures A3–A12 in Appendix A. Generally, we do not find significant H I detection except for those from the ISM of IC 1613 as probed by stellar sight lines S1–S4.

3. Absorbers in the Rest Frame of IC 1613

In this section, we investigate the ion absorbers' physical connection with IC 1613, as all the sight lines (S1–S4, Q1–Q6) are within $0.6R_{200}$ of the galaxy (see Figure 1). We defer the discussion of potential foreground contamination to Section 4. The distances to these absorbers are unknown except for their impact parameters with respect to IC 1613; therefore, our diagnosis is based on other measurements such as velocities and line widths.

From Figure 2 and Table 3, we find that Si II, Si III, Si IV, C II, and C IV absorption are strong and commonly detected among the stars S1–S4; origins for the absorption include the ISM of IC 1613 ($v_{\mathrm{IC\ 1613}} \sim 0\,\mathrm{km\,s^{-1}}$), potential inflows ($v_{\mathrm{IC\ 1613}} > 0\,\mathrm{km\,s^{-1}}$) and outflows ($v_{\mathrm{IC\ 1613}} < 0\,\mathrm{km\,s^{-1}}$), and the galaxy's CGM ($|v_{\mathrm{IC\ 1613}}| < v_\mathrm{esc}$), where v_esc means the escape velocity of the galaxy and $v_{\mathrm{IC\ 1613}}$ means the velocity is relative to IC 1613's systemic velocity. Toward the QSO sight lines Q1–Q6, absorbers appear to be weaker and the line strengths vary from sight line to sight line; they are likely to originate in the CGM of IC 1613 if $|v_{\mathrm{IC\ 1613}}| < v_\mathrm{esc}$. Based on the ion absorbers' positions and velocities relative to IC 1613 and the line quality, we assign different tags to the absorbers tabulated in Table 3 as follows.

Origin tag = "CGM": absorbers detected along Q1–Q6 that are most likely to originate in the CGM of IC 1613. The velocities of these absorbers are $|v_{\mathrm{IC\ 1613}}| < |v_\mathrm{esc}| - 20\,\mathrm{km\,s^{-1}}$, where the $20\,\mathrm{km\,s^{-1}}$ value is to account for the COS spectral uncertainty.

Origin tag = "CGM/Outflow" or "CGM/Inflow": absorbers detected along S1–S4 that are most likely to be either in the CGM of IC 1613 or outflows or inflows near the galaxy. The

Table 3
Absorber Measurements

Ion	Method	$v_{\rm IC\ 1613}$ (km s^{-1})	b (km s^{-1})	log N log(cm^{-2})	W_r (mÅ)	Origin Tag
(1)	(2)	(3)	(4)	(5)	(6)	(7)
S1: IC 1613-C10 ($v_{\rm sys} = -239.4$ km s^{-1})[a]						
C II	VP	−99.7 ± 1.8	19.1 ± 3.0	14.07 ± 0.04	126.2 ± 7.9	CGM/Outflow
	VP	−51.8 ± 1.9	11.5 ± 3.9	13.90 ± 0.07	100.4 ± 5.0	CGM/Outflow
	VP	1.0 ± 1.7	22.5 ± 3.4	14.42 ± 0.04	258.7 ± 7.2	ISM
	VP	65.9 ± 7.8	25.8 ± 14.7	13.59 ± 0.19	73.0 ± 7.1	CGM/Inflow
Si II	VP	−90.7 ± 2.3	18.9 ± 3.6	13.02 ± 0.04	40.8 ± 7.6	CGM/Outflow
	VP	−40.8 ± 2.5	17.8 ± 4.6	12.94 ± 0.07	61.6 ± 7.1	CGM/Outflow
	VP	13.6 ± 0.6	11.0 ± 0.8	14.00 ± 0.08	109.3 ± 6.8	ISM
S2: IC 1613-B7 ($v_{\rm sys} = -234.3$ km s^{-1})[a]						
C II	VP	−138.9 ± 8.5	39.2 ± 12.4	13.70 ± 0.10	77.7 ± 8.1	Non-Association
	VP	−68.4 ± 2.7	21.4 ± 4.6	14.13 ± 0.07	172.1 ± 5.2	CGM/Outflow
	VP	−9.3 ± 1.8	25.3 ± 2.4	14.63 ± 0.04	282.5 ± 6.0	ISM
Si II	VP	−55.7 ± 1.5	13.1 ± 2.7	13.60 ± 0.05	160.0 ± 11.4[b]	CGM/Outflow
	VP	−2.0 ± 0.8	17.9 ± 2.0	14.64 ± 0.15	445.8 ± 11.6[b]	ISM
Si III	VP	−132.4 ± 8.6	15.4 ± 12.6	12.43 ± 0.26	42.9 ± 9.2	Non-Association
	VP	−73.1 ± 5.5	31.4 ± 12.8	13.15 ± 0.12	169.0 ± 7.7	CGM/Outflow
	VP	−9.5 ± 3.2	23.3 ± 4.6	13.35 ± 0.05	213.6 ± 5.0	ISM
	VP	54.4 ± 8.2	16.1 ± 15.7	12.23 ± 0.26	50.9 ± 7.2	CGM/Inflow
S3: IC 1613-A13 ($v_{\rm sys} = -231.7$ km s^{-1})[a]						
C II	VP	−66.7 ± 43.9	43.2 ± 37.6	13.65 ± 0.52	49.5 ± 9.4	CGM/Outflow
	VP	−7.2 ± 3.2	27.9 ± 3.4	14.61 ± 0.07	324.2 ± 8.3	ISM
Si II	VP	−9.5 ± 0.6	19.0 ± 0.9	14.30 ± 0.04	237.2 ± 8.6	ISM
Si III	VP	−81.6 ± 7.7	28.1 ± 9.2	12.89 ± 0.12	169.1 ± 7.8	CGM/Outflow
	VP	−15.7 ± 2.9	28.5 ± 3.4	13.55 ± 0.05	229.3 ± 6.4	ISM
C IV	VP	−94.5 ± 4.5	25.1 ± 7.0	13.45 ± 0.10	79.4 ± 7.9	CGM/Outflow
	VP	−18.0 ± 1.7	36.0 ± 2.4	14.17 ± 0.02	303.6 ± 10.0	ISM
S4: IC 1613-B11 ($v_{\rm sys} = -242.0$ km s^{-1})[a]						
C II	VP	−120.0 ± 6.3	20.6 ± 10.0	13.44 ± 0.12	62.6 ± 10.7	Non-Association
	VP	−21.6 ± 1.6	37.8 ± 2.5	14.64 ± 0.03	374.4 ± 11.5	CGM/Outflow
Si II	VP	−33.6 ± 10.1	41.4 ± 6.6	13.44 ± 0.13	95.9 ± 9.3	CGM/Outflow
	VP	−3.6 ± 0.9	12.2 ± 1.9	14.33 ± 0.17	164.9 ± 8.1	ISM
Si III	VP	−64.2 ± 14.6	35.2 ± 10.6	13.39 ± 0.24	242.7 ± 8.9	CGM/Outflow
	VP	−1.1 ± 12.1	36.4 ± 8.7	13.53 ± 0.18	300.8 ± 9.7	ISM
C IV	VP	−49.9 ± 11.1	45.5 ± 16.5	13.46 ± 0.11	51.1 ± 20.1	CGM/Outflow
Q1: LBQS-0100+0205 ($v_{\rm sys} = -236$ km s^{-1})[a]						
C II	AOD	[−70, 20]	···	<13.74	<48.9	Non-Detection
Si II	AOD	[−50, 50]	···	<13.03	<49.8	Non-Detection
Si III	VP	0.7 ± 3.4	25.1 ± 5.2	12.96 ± 0.06	126.2 ± 16.6	CGM
Si IV	VP	−21.2 ± 5.8	37.1 ± 8.8	13.00 ± 0.07	65.6 ± 13.2	CGM
C IV	AOD	[−70, 50]	···	13.57 ± 0.09	117.3 ± 27.5	CGM
Q2: LBQS-0101+0009 ($v_{\rm sys} = -236$ km s^{-1})[a]						
C II	VP	−19.3 ± 2.1	23.6 ± 3.1	14.21 ± 0.05	189.9 ± 14.8	CGM
Si II	VP	−12.0 ± 4.3	30.0 ± 5.4	13.19 ± 0.06	77.8 ± 16.1	CGM
Si III	VP	−14.8 ± 4.5	50.1 ± 6.2	13.30 ± 0.05	271.3 ± 23.1	CGM
Si IV	AOD	[−50, 50]	···	<12.79	<35.1	Non-Detection

Table 3
(Continued)

Ion	Method	$v_{\rm IC\ 1613}$ (km s^{-1})	b (km s^{-1})	log N log(cm^{-2})	W_r (mÅ)	Origin Tag
(1)	(2)	(3)	(4)	(5)	(6)	(7)
C IV	AOD	[−40, 75]	···	13.64 ± 0.07	144.4 ± 23.2	CGM
Q3: 2MASX-J0102-0039 ($v_{\rm sys}$ = −236 km s^{-1})[a]						
C II	VP	−31.1 ± 2.2	23.3 ± 3.0	14.28 ± 0.05	205.5 ± 9.5	CGM
	VP	43.5 ± 5.7	44.4 ± 8.0	14.15 ± 0.06	185.2 ± 9.9	CGM
Si II	VP	−23.5 ± 1.4	24.0 ± 2.1	13.48 ± 0.03	124.1 ± 12.0	CGM
	VP	61.4 ± 2.5	13.0 ± 4.4	12.85 ± 0.07	59.2 ± 11.9	CGM
Si III	VP	−31.9 ± 2.9	20.7 ± 4.4	13.19 ± 0.07	176.3 ± 13.8	CGM
	VP	40.1 ± 9.2	42.8 ± 13.9	12.92 ± 0.09	123.1 ± 10.8	CGM
Si IV	AOD	[−90, 60]	···	13.02 ± 0.07	84.0 ± 15.1	CGM
C IV	AOD	[−90, 80]	···	13.78 ± 0.05	205.7 ± 22.4	CGM
Q4: PG0044+030 ($v_{\rm sys}$ = −236 km s^{-1})[a], G130M-only						
C II	VP	−58.6 ± 3.4	22.4 ± 5.7	14.01 ± 0.07	135.0 ± 18.0	Non-Association[c]
	VP	23.4 ± 5.7	29.5 ± 9.0	13.89 ± 0.09	116.7 ± 15.8	CGM
Si II	AOD	[−100, 20]	···	13.31 ± 0.10	102.5 ± 25.2	CGM
Si III	VP	−49.9 ± 4.7	34.5 ± 7.5	13.26 ± 0.07	229.8 ± 21.4	CGM
	VP	36.3 ± 4.6	13.4 ± 8.0	12.79 ± 0.16	89.1 ± 17.4	CGM
Si IV	AOD	[−50, 50]	···	<13.00	<68.7	Non-Detection
Q5: HB89-0107-025-NED05 ($v_{\rm sys}$ = −236 km s^{-1})[a]						
C II	AOD	[−50, 50]	···	<13.38	<29.7	Non-Detection
Si II	AOD	[−50, 50]	···	<13.04	<38.7	Non-Detection
Si III	AOD	[−50, 50]	···	12.76 ± 0.06	100.7 ± 14.0	CGM
Si IV	AOD	[−50, 50]	···	<13.02	<34.2	Non-Detection
C IV	AOD	[−50, 50]	···	13.56 ± 0.06	121.5 ± 15.9	CGM
Q6: LBQS-0107-0235 ($v_{\rm sys}$ = −236 km s^{-1})[a]						
C II	AOD	[−50, 80]	···	13.60 ± 0.08	71.3 ± 14.0	CGM
Si II	AOD	[−100, 100]	···	13.30 ± 0.07	111.0 ± 17.7	CGM
Si III	AOD	[−70, 75]	···	12.77 ± 0.06	105.1 ± 15.4	CGM
Si IV	AOD	[−50, 50]	···	<12.80	<42.6	Non-Detection
C IV	VP	−26.8 ± 3.7	47.9 ± 5.3	13.91 ± 0.04	221.5 ± 10.7	CGM
	VP	57.6 ± 6.7	25.9 ± 9.7	13.24 ± 0.13	64.8 ± 8.4	Non-Association[c]

Notes. Column (2): if Method = VP, the measurements are from Voigt-profile fits. If Method = AOD where the lines either do not yield robust Voigt-profile fits or there is no detection, we use Si II 1193, Si III 1206, Si IV 1393, C II 1334, and C IV 1548 to integrate for the AOD values. We do not use the stronger Si II 1260 line because it is contaminated by the S II 1259 line from the Milky Way. Column (3): if Method = VP, $v_{\rm IC\ 1613}$ indicates the fitted centroid velocity in the rest frame of IC 1613. If Method = AOD, $v_{\rm IC\ 1613}$ shows a velocity range as used in the AOD integration. Column (4): if Method = VP, b indicates the fitted Doppler width. No value is available if Method = AOD. Column (5): if Method = VP, log N indicates the fitted column density. If Method = AOD, log N is estimated based the AOD method. We report a 3σ upper limit if there is no detection as is often the case in Q1–Q6. Column (6): equivalent width integrated over the same velocity range as the log N. We report 3σ upper limits for nondetection. Column (7): origins of absorbers in the context of IC 1613 as identified in Section 3.

Other notes:

[a] $v_{\rm sys}$ is the systemic velocity of the galaxy at the position of the sight line. For S1–S4, $v_{\rm sys}$ is estimated based on the peak emission of H I 21 cm emission (see Section 2.3). For Q1–Q6, $v_{\rm sys} = v_{\rm LSR} = -236$ km s^{-1} (see Table 1).

[b] Si II 1193 in S2 is contaminated and does not yield good fit if included in the fitting, so we estimate $W_{\rm r}$ from Si II 1190, and convert the value to Si II 1193's with $W_{\rm r}(1193) = W_{\rm r}(1190)\frac{f_{1193}\lambda^2_{1193}}{f_{1190}\lambda^2_{1190}}$, where f and λ are the oscillator strength and wavelength, respectively.

[c] We consider this absorber to be a Non-Association because its $v_{\rm IC\ 1613}$ value is ∼20 km s^{-1} (19.6 km s^{-1} for Q4/C II and 20.3 km s^{-1} for Q6/C IV) from the escape velocity at the corresponding impact parameter. Given the velocity uncertainty of COS (adopted as 20 km s^{-1} in this work) and the uncertainty of the absorber's centroid velocity (∼5 km s^{-1}), we conservatively tag it as Non-Association but do not rule out its possibility to be related to IC 1613 .

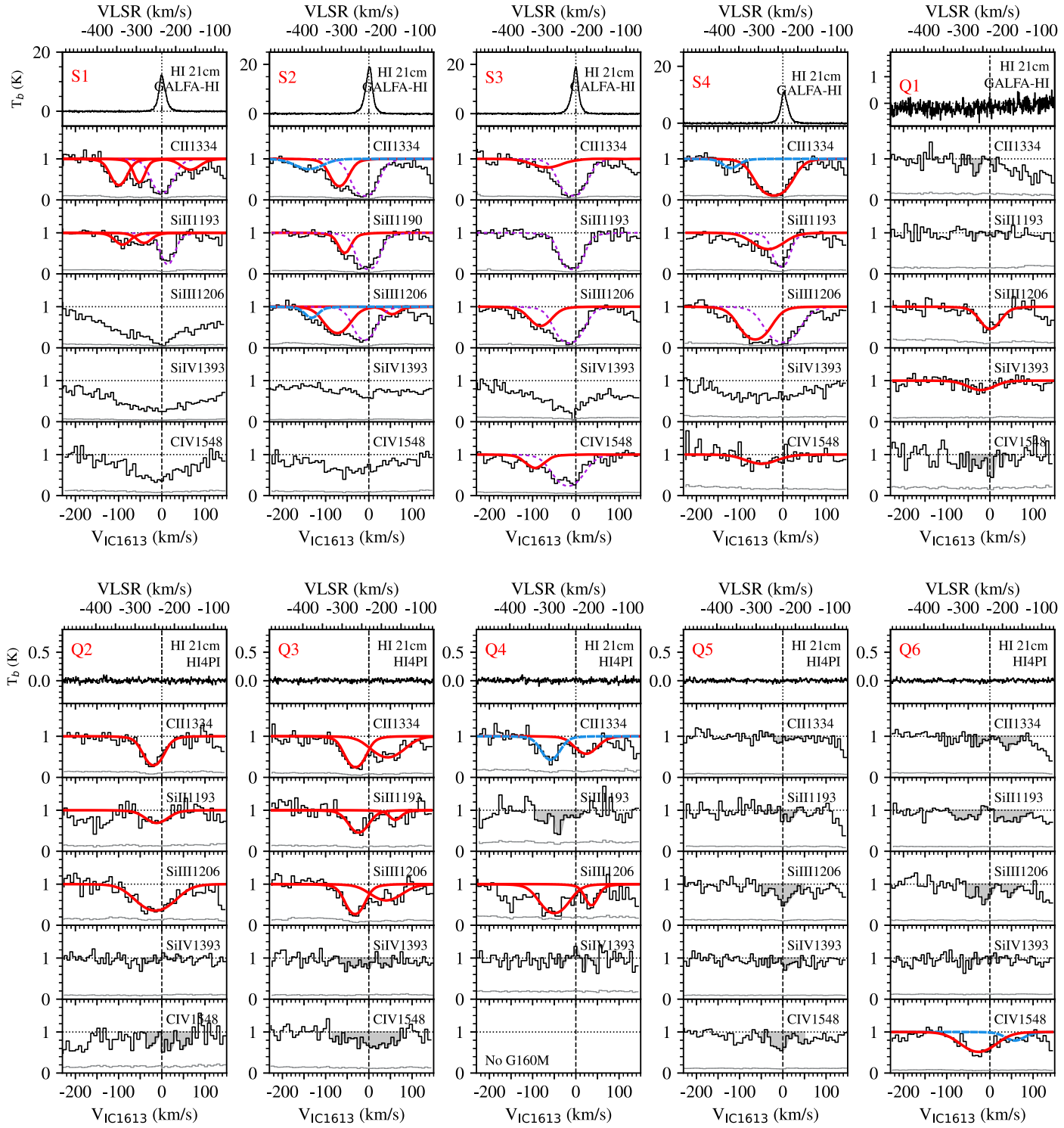

Figure 2. H I 21 cm emission and metal ion absorption lines measured toward S1–S4 and Q1–Q6. All of the spectra are plotted in the LSR (v_{LSR}, top *X*-axes) and in the rest frame of IC 1613 ($v_{IC\ 1613}$, bottom *X*-axes). We only show a subset of the ion lines in this figure and include the full set of ion multiplets in Figures A3–A12 in Appendix A. The red solid curves show the Voigt-profile components that are considered to be associated with IC 1613 (i.e., "CGM," "CGM/Inflow," "CGM/Outflow" in Table 3). The purple dotted curves indicate IC 1613's ISM components, and the blue curves show absorbers that are unlikely to be related to IC 1613 (i.e., "Non-Association"). Toward Q1–Q6, when the Voigt-profile fitting does not yield robust results because of low spectra S/N, we estimate the AOD column density with velocity integrated over the gray-shaded regions. The vertical line in each panel shows the systemic velocity of IC 1613 . For S1–S4, the galaxy's systemic velocity is estimated based on the peak H I emission from VLA (see Section 2.3 and Figures A3–A6) toward the corresponding sight line; for Q1–Q6, it is $v_{LSR} = -236$ km s^{-1} as listed in Table 1. For S2, we show the Si II 1190 line instead of the 1193 one because the latter is blended with an unknown feature and it does not yield reasonable Voigt-profile fits if included.

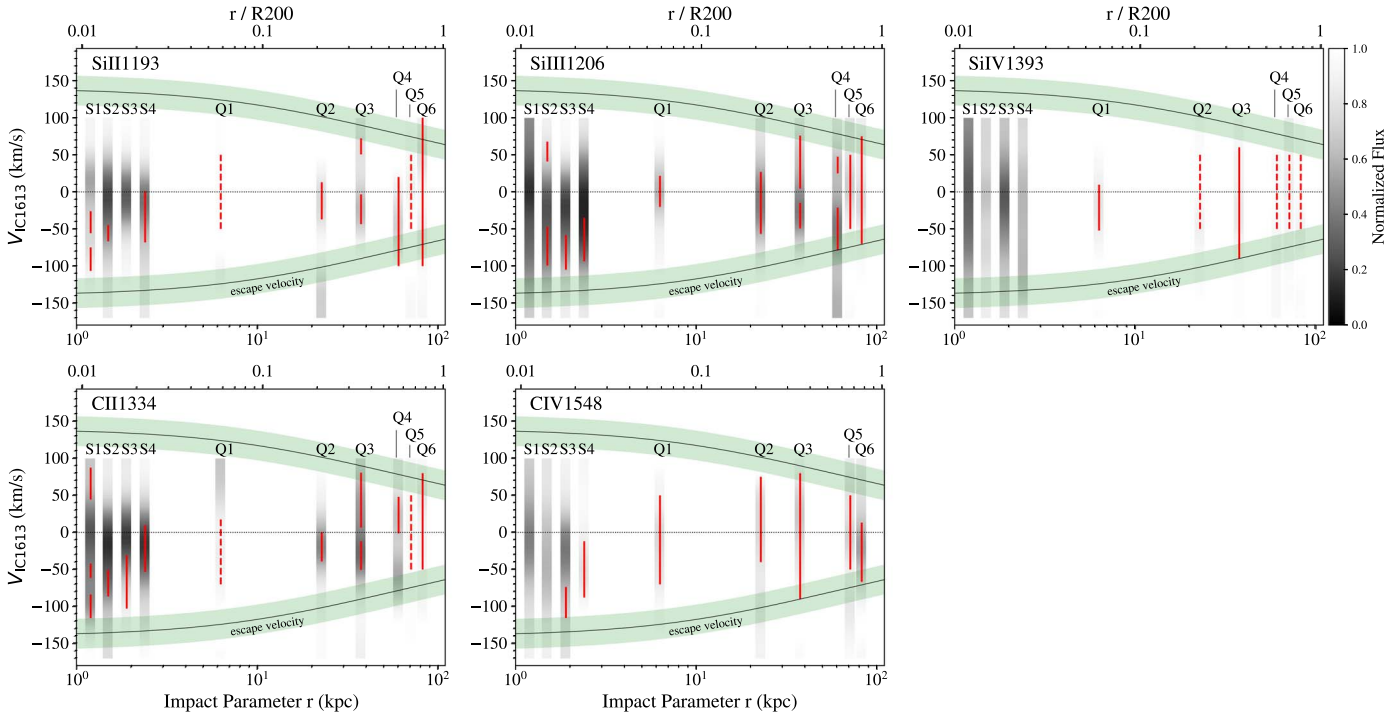

Figure 3. Ion absorbers that are most likely to be associated with IC 1613. They are measurements tagged as "CGM," "CGM/Outflow," "CGM/Inflow," or "Non-Detection" in Table 3 and Section 3. The red solid lines show the FWHM (=1.667*b*) of the Voigt-profile fits or the AOD velocity integration ranges of the detected absorbers, and the red dashed lines are for the nondetection 3σ upper limit ranges. For each target, the gray band shows the continuum-normalized line profile, with dark gray indicating strong absorption and vice versa. The green shades are escape velocities with 20 km s^{-1} uncertainty due to the COS spectral resolution. Stars S1–S4 are inside the galaxy; we place them at arbitrary but small r to separate one from another. Q4–Q6 have similar impact parameters ($r \sim 61$ kpc; Table 2); we manually separate the gray bands slightly for better illustration.

ambiguity of the absorbers' locations is because these stellar sight lines are observed in a down-the-barrel manner. Specifically, absorbers with $v_{\rm esc} + 20 < v_{\rm IC\ 1613} < -20$ km s^{-1} are tagged as "'CGM/Outflow," and those with $20 < v_{\rm IC\ 1613} < v_{\rm esc} - 20$ km s^{-1} are "CGM/Inflow."

Origin tag = "Non-Detection": there is no detection of absorption within the designated velocity ranges. This tag is only for Q1–Q6, and we provide 3σ upper limits on the column densities and the equivalent widths.

Origin tag = "ISM": absorbers detected along S1–S4 that are likely to be in the ISM of IC 1613, with $|v_{\rm IC\ 1613}| < 20$ km s^{-1}. Their Voigt profiles are shown in purple dotted curves in Figure 2, which tend to be broader and stronger than the non-ISM components. We do not use these absorbers in our analyses.

Origin tag = "Non-Association": absorbers that are unlikely to be associated with IC 1613 because they are not gravitationally bound, $|v_{\rm IC\ 1613}| > |v_{\rm esc}| - 20$ km s^{-1}. The Voigt profiles of these absorbers are shown in blue curves in Figure 2, which tend to be much weaker than other IC 1613-associated counterparts. We do not use these absorbers in our analyses regarding the CGM metal content and outflows of IC 1613.

Based on this tagging system, we show in Figure 3 the impact parameters and velocities of the absorbers tagged with "CGM," "CGM/Outflow," "CGM/Inflow," or "Non-Detection" in the rest frame of IC 1613. We also show the original line spectra as vertical gray bands to highlight the spread of the ion absorption. By design, the ion absorbers likely to be associated with IC 1613 have velocities clustered within $\sim\pm100$ km s^{-1}, as limited by the range of the escape velocity. While it is necessary to use escape velocity to constrain whether an absorber is related to IC 1613 given the complex gaseous environment in the LG (see Section 4), we note that IC 1613 may have high-velocity outflows that are not gravitationally bound escaping the disk (i.e., $v_{\rm IC\ 1613} > v_{\rm esc}$). Such outflows would not be recognized as "CGM/Outflow" based on our criterion. Therefore, our estimates of the mean outflow velocities and other relevant properties (see Section 5.3) should be considered as conservative lower limits.

The mean velocities of the "CGM/Outflow" absorbers are -45 ± 20 km s^{-1} for Si II, -71 ± 8 km s^{-1} for Si III, -66 ± 10 km s^{-1} for C II, and -63 ± 20 km s^{-1} for C IV, respectively. The mean values are weighed by the measurement errors, and the uncertainties are the standard deviations of the velocities also weighted by the measurement errors. If corrected for the inclination of the galaxy ($\theta = 37.^{\circ}9$; see Table 1) and assuming that outflows are perpendicular to the galaxy's disk, the mean outflow velocity for each ion would increase by $1/\cos\theta = 1.3$. Despite there being detection of broad Si IV absorption lines in all the stellar sight lines, we do not have an outflow velocity value for Si IV because there is no robust Voigt-profile fit that can separate the ISM from the non-ISM components.

The detection rate (or covering fraction) C_f of the "CGM," "CGM/Outflow," "CGM/Inflow," and "Non-Detection" absorbers within $0.6R_{200}$ is 82% (9/11) for Si II, 100% (12/12) for Si III, 33% (2/6) for Si IV, 85% (11/13) for C II, and 100% (7/7) for C IV, respectively. And the detection limit for these ions is generally $W_{\rm r} \gtrsim 50$ mÅ, although note that the detection limit

depends on the spectral S/N. The mean column densities (as weighted by measurement errors) are 13.24 ± 0.04 dex for Si II, 12.91 ± 0.07 dex for Si III, 13.01 ± 0.05 dex for Si IV, 13.80 ± 0.22 dex for C II, and 13.51 ± 0.04 dex for C IV, respectively.

Lastly, the error-weighted mean Doppler width (b) and its standard deviation is $32 \pm 11\,\mathrm{km\,s^{-1}}$ for all the Voigt-profile fitted components tagged as "CGM," "CGM/Outflow," and "CGM/Inflow." The b value changes by $<10\,\mathrm{km\,s^{-1}}$ if we focus on a specific ion or outflow-only absorbers. Our derived b values are consistent with those of Si III and C IV measured toward two field dwarf galaxies (D1 and D2) with QSO sight lines at $<0.2R_{200}$[10] by Johnson et al. (2017), and they are on average larger than the b values measured for the ionized gas near the Magellanic Stream ($b < 25\,\mathrm{km\,s^{-1}}$ Fox et al. 2020), suggesting that our absorbers are unlikely to be associated with the Stream. We discuss in more detail how the foreground Magellanic Stream impacts our diagnosis of the ion absorbers' origins in Section 4.

4. The Magellanic System in the Foreground

Hereafter, we refer to the LMC/SMC, the Magellanic Stream, the Magellanic Bridge, and the Leading Arm as the Magellanic System. In Figure 4, we show the Magellanic System in the so-called Magellanic Stream Coordinate System ($L_{\rm MS}$, $B_{\rm MS}$; Nidever et al. 2008), where the equator ($B_{\rm MS} = 0°$) bisects the spine of the Stream and the LMC is at $L_{\rm MS} = 0°$. IC 1613 is located near the tail of the Stream at $L_{\rm MS} = -84.^{\circ}1$, $B_{\rm MS} = 21.^{\circ}5$. It is isolated from other galaxies in the LG and $\sim 20°$ from the Magellanic Stream in projection.

The Magellanic System has been widely detected in H I 21 cm (Mathewson et al. 1974; Putman et al. 1998, 2003; Nidever et al. 2008) and occupies $\sim$2700 square at $\mathrm{N(H\,I)} \geqslant 10^{18}$ $\mathrm{cm^{-2}}$ (Nidever et al. 2010; D'Onghia & Fox 2016). Hα emission from the Magellanic Stream is observed by WHAM (Haffner et al. 2003) to extend $\sim 2°$ from the Magellanic H I-bright regions (Barger et al. 2017). Ionized gas detected via UV absorption lines is thought to be distributed out to 30° from the H I, with a cross section of $\approx$11,000 $\mathrm{deg^2}$, with the assumption that the ionized gas associated with the Magellanic System should have a line-of-sight velocity ($v_{\rm LSR}$) aligned with the H I at a given $L_{\rm MS}$ (Fox et al. 2014, hereafter Fox14; Richter et al. 2017). This is to say the ionized and neutral gas of the Magellanic System are assumed to occupy the same parameter space in the position ($L_{\rm MS}$)—velocity ($v_{\rm LSR}$) diagram. Here we examine this position–velocity criterion in the context of the CGM of IC 1613.

In the top panel of Figure 4, in red and blue colors we show the velocity ($v_{\rm LSR}$) of the Magellanic System's H I emission Gaussian-fitted components (Nidever et al. 2008) as well as the positions of some LG galaxies (see below for selection criteria of these galaxies). The white area in this top panel shows the ionized cross section of the Magellanic System defined by Fox14; within this cross section, 81% (56/69) of their QSO sight lines (not shown here) are detected with ion absorbers that are identified as Magellanic. We show these ion absorbers (blue) in the bottom panel on the $L_{\rm MS}$–$v_{\rm LSR}$ diagram, which are indeed aligned with the Magellanic H I emission (gray). We also overlay ion absorbers detected near IC 1613 (red) in this bottom panel, which appear to be largely consistent with the location of the Magellanic H I. Furthermore, Lehner et al. (2020) find that 38% (28/74) of their detected Si III absorbers toward M31 are aligned with the Magellanic H I emission (magenta).

As we investigate further, we find that an absorber's alignment with the Magellanic H I on the $L_{\rm MS}$–$v_{\rm LSR}$ diagram does not necessarily lead to a physical connection between the two. To demonstrate this, in the middle panel, we show a number of galaxies in the LG that are near the Magellanic System in projection but are not physically connected to it. These galaxies are selected from the dwarf galaxy catalog compiled by Putman et al. (2020, submitted), and we also include four more massive LG members (M31, M33, NGC 55, and NGC 300). We only consider LG galaxies that are (1) within distance $d_{\odot} > 300$ kpc from the Sun and (2) have line-of-sight velocities. Criterion (1) is to exclude Milky Way satellites that could be considered physically associated with the Magellanic System based on proper motions and orbital history studies (e.g., Patel et al. 2020). Criterion (2) is a necessity for the $L_{\rm MS}$–$v_{\rm LSR}$ diagram.

With criteria (1) and (2), we find 81 LG galaxies near the Magellanic System in position–velocity space despite them not being physically connected. In the middle panel, we calculate the separation between the LG galaxies and their closest H I emission Gaussian components of the Magellanic System and find that 73% (59/81) of these galaxies are coincidentally aligned with the Magellanic System within $10\,\mathrm{km\,s^{-1}}$ in $v_{\rm LSR}$ and 1° in $L_{\rm MS}$ and $B_{\rm MS}$. Without the prior knowledge of the distances to these LG galaxies (all at $d_{\odot} > 300$ kpc), one may wrongly conclude that they are physically associated with the Magellanic System. Therefore, we argue that the alignment of an object with the Magellanic H I on the $L_{\rm MS}$–$v_{\rm LSR}$ diagram does not provide solid evidence that the object originated from the System.

Because of the coincident alignment between the LG galaxies and the Magellanic System, we further show that potential CGM absorbers originated from H I-rich galaxies in the LG will appear in a similar $L_{\rm MS}$–$v_{\rm LSR}$ parameter space, further complicating the diagnosis of an absorber's origin. Because such an investigation is beyond the context of IC 1613's CGM, we defer the relevant analysis to Appendix B to keep the main text focusing on IC 1613. Briefly, in Appendix B, we calculate the angular extent of the CGM of H I-rich dwarf galaxies selected based on Criteria (1) and (2) and show that the total cross section of these galaxies' CGM is nonnegligible.

To conclude, we argue that the angular extent of the ionized cross section of the Magellanic System should be revisited using more robust methods other than the $L_{\rm MS}$–$v_{\rm LSR}$ diagram. For example, a recent hydrodynamic simulation of the Magellanic System by Lucchini et al. (2020) predicts a broad ionized component encompassing both the Leading Arm and Magellanic Stream due to the interaction between a massive LMC corona with the Milky Way's CGM. They suggest that the column densities of the LMC-associated, highly ionized gas should decrease with increasing impact parameters. It remains to be determined whether such a decreasing trend in column density can aid in better defining the angular extent of the Magellanic System. On the other hand, the ionized gas of the Magellanic System is likely to be confused with the CGM of H I-rich LG galaxies if the QSO sight lines are within the galaxies' virial radii (see

[10] The virial radii of Johnson et al.'s (2017) galaxies have been recalculated to be consistent with our definition of R_{200} using the galaxies' stellar masses (see Section 6.1).

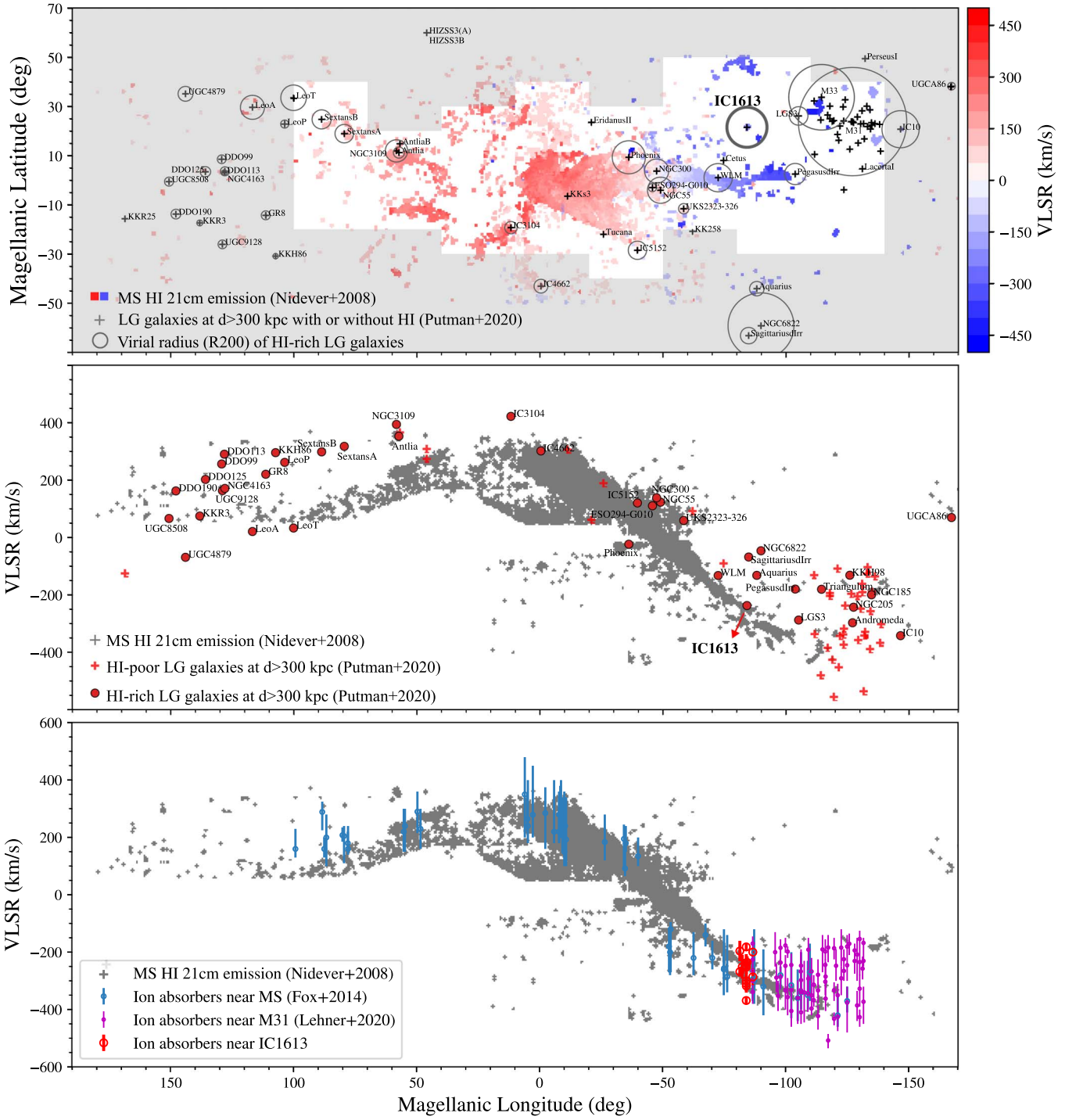

Figure 4. Top: 81 LG galaxies with $d_{\odot} > 300$ kpc (crosses; Putman et al. 2020, submitted) that are not physically connected to the Magellanic System (red and blue colors; Nidever et al. 2008). The LG galaxies include 77 dwarf galaxies and 4 more massive ones (M31, M33, NGC 55, and NGC 300). Data are shown in the Magellanic Coordinate system (Nidever et al. 2008; *gala* package, Price-Whelan et al. 2017). For clarity, the names of the dwarfs clustering near M31 are not shown. The white region represents the ionized cross section of the Magellanic System as identified by Fox14. The virial radii (R_{200}) of H I-rich galaxies are indicated as black circles, which are used to determine the angular extent of their CGM (see Appendix B). Middle: coincident alignment between LG galaxies (red symbols) and the Magellanic H I emission (gray dots; Nidever et al. 2008) on the position–velocity diagram. Bottom: similar coincident alignment between ion absorbers near IC 1613 (red open circle; this work), M31 (magenta; Lehner et al. 2020), and the Magellanic H I-emitting region (blue; Fox14). For data points from Fox14 and Lehner et al. (2020), the vertical bars show the minimum and maximum velocities used in their AOD measurements. For IC 1613's, we show Si III's centroid velocities and the FWHM ($\equiv 1.667b$). The middle and bottom panels show that an absorber's alignment with the Magellanic System does not necessarily lead to a physical connection between the two, and the angular extent of the Magellanic System's ionized gas should be revisited with more robust methods other than this position–velocity diagram.

Appendix B). In the case of IC 1613, as we discussed in Section 1 and Section 3, the detected absorbers are most likely to be associated with the CGM of IC 1613 given the star formation history of the galaxy, the proximity of the absorbers to the galaxy, and the larger b values of the ion absorbers than other ionized gas near the Stream.

5. The Metal Mass Budget and Mass Loading Factor of IC 1613

In Section 3, we have identified ion absorbers that are most likely to be associated with IC 1613. Here, we will use the measurements of these absorbers to empirically estimate the silicon (Si) mass budget in the star, ISM, and CGM of IC 1613 (see Section 5.1), and then compare our estimates to predicted values from simulations (see Section 5.2). We will further estimate the metal outflow rate and the instantaneous metal mass loading factor in Section 5.3.

5.1. Metal Mass Budget Estimate

Given that there is no detection of H I among the QSO sight lines (see Figure 2), the CGM of IC 1613 is likely to be fully ionized. We first estimate the total Si mass in the CGM assuming that Si II, Si III, and Si IV comprise nearly 100% of the total Si and leveraging the fact that these ions are simultaneously detected in the COS spectra. We only use absorbers tagged as "CGM" from Q1–Q6 in Table 3. We decide to exclude potential CGM absorbers detected in S1–S4 (i.e., those tagged as "CGM/Outflow" or "CGM/Inflow") because their impact parameters from the galaxy are ambiguous as the stellar sight lines were observed in a down-the-barrel manner. We note that including these absorbers would not change our mass estimate significantly.[11]

We follow the same methodology as outlined in Section 4 of Zheng et al. (2019b; hereafter Zheng19) which estimated Si mass budget for the dwarf irregular galaxy WLM. The main difference from Zheng19 is that here we are able to integrate the Si mass radially based on data from Q1–Q6, without assuming a radial profile or covering fraction. By taking each absorber to represent the azimuthal average of concentric annuli around IC 1613, the total Si mass can be derived as

$$M_{\rm Si}^{\rm CGM}(\leqslant 0.6R_{200}) = \sum \pi (r_k^2 - r_{k-1}^2) m_{\rm Si} N_{\rm Si,k} \approx (1.0\text{–}1.3) \times 10^5\, M_\odot, \quad (1)$$

where $m_{\rm Si}$ is the mass of a Si atom, r_k is the impact parameter of each QSO with k corresponding to the QSO's ID number in Table 2, and r_0 is set as 0. Along each sight line, we have $N_{\rm Si,k} = N_{\rm SiII,k} + N_{\rm SiIII,k} + N_{\rm SiIV,k}$. In Table 4, we record the Si mass estimated for each (r_{k-1}, r_k) annulus, as well as the Si mass locked in the stars and ISM as estimated below.

Same as Zheng19, we adopt $R = 0.34$ for the fraction of mass returned to the ISM per stellar generation, and $R_* = 1 - R = M_*/M_{\rm tot,SF} = 0.66$ for the fraction locked in stars since star formation, where $M_{\rm tot,SF}$ is the total mass formed with star formation. The stellar yield is $y_{\rm Si} \equiv M_{\rm Si}^{\rm gas}/M_* = 0.003$, which is the ratio of the Si mass in gas to the total stellar mass. The R and $y_{\rm Si}$ values were initially derived for WLM with the NuGrid collaboration yield set and the SYGMA simple stellar population model (Ritter et al. 2018a, 2018b), which are applicable to IC 1613 given that the two galaxies have similar gas-phase metallicity. Below we follow Zheng19's Equations (3)–(7) to derive relevant Si masses, but refrain from explaining the details that go into each calculation.

Table 4
Silicon Mass Fraction Radial Profile

r (kpc) (1)	Component (2)	$M_{\rm si}/10^3\, M_\odot$ (3)	$M_{\rm si}/M_{\rm Si}^{\rm tot}$ (4)
0	stars	∼8	3%
0	ISM	∼7	2%
(0, 6]	CGM (<Q1)	∼(0.5–0.8)	0.2%–0.3%
(6, 23]	CGM (Q1–Q2)	∼(12–14)	4%–5%
(23, 38]	CGM (Q2–Q3)	∼(40–50)	13%–16%
(38, 61]	CGM (Q3–Q456)	∼(48–62)	15%–20%
(0, 61]	CGM (<0.6R_{200})	∼(100–130)	32%–42%

Note. Column (1): the impact parameter at which the Si mass is calculated. Column (2): for the Si mass in the stars and ISM, we follow the same procedures outlined in Zheng19; the Si mass in the CGM probed by each QSO is computed with Equation (1) without doing the total sum. Column (3): for the CGM Si mass measured toward Q1–Q6, a mass range is given with the left bound estimated with "CGM" absorbers and the right bound with both "CGM" and "Non-Detection" absorbers for the 3σ upper limit. Because the impact parameters of Q4–Q6 are very similar, we use the average of their impact parameters for r_4 and the corresponding mean column densities for $N_{\rm Si,4}$ in Equation (1). Column (4): Si mass fraction in the stars, ISM, and CGM related to the total amount of Si ever produced (see Section 5.1).

The total Si mass in the gas, including those in the ISM, CGM, or beyond, is $M_{\rm Si}^{\rm gas} = y_{\rm Si} M_* = 0.003 \times 10^8\, M_\odot = 3 \times 10^5\, M_\odot$. The relative abundance of Si to H in IC 1613's ISM is $12 + \log({\rm Si/H})_{\rm IC1613} = 6.55 \pm 0.07$,[12] with which we can infer the Si mass in IC 1613's ISM as $M_{\rm Si}^{\rm ISM} = M_{\rm HI}(m_{\rm Si}/m_{\rm H})({\rm Si/H})_{\rm IC1613} \sim 7 \times 10^3\, M_\odot$. Similarly, we can estimate the total amount of Si locked in the stars as $M_{\rm Si}^* = 0.74 M_*(m_{\rm Si}/m_{\rm H})({\rm Si/H})_{\rm IC1613} \sim 8 \times 10^3\, M_\odot$, where 0.74 is the hydrogen mass fraction.

The total amount of Si ever produced in IC 1613 is $M_{\rm Si}^{\rm tot} = M_{\rm Si}^* + M_{\rm Si}^{\rm gas} \approx 3.1 \times 10^5\, M_\odot$. When considering the Si mass fraction, we find that ∼3%, ∼2%, and ∼32%–42% of the mass is in the stars, ISM, and within 0.6R_{200} of the CGM, respectively. In Figure 5, we show the cumulative Si mass fraction in IC 1613 and its CGM. At $d \sim 0$ kpc, the galaxy itself contains ∼5% of the Si in the stars and ISM. In the CGM, the Si mass fraction increases quickly with r mainly because the mass is proportional to the surface area $\propto r^2$ (see Equation (1)).

5.2. Mass Budget Comparison with Simulations

In Figure 6, we compare the Si mass budgets for IC 1613 and WLM (Zheng19) to the predicted values for dwarf galaxies with $M_* \sim 10^6$–$10^{10}\, M_\odot$ from the FIRE and FIRE2 simulations as analyzed in Muratov et al. (2017) and Hafen et al. (2019), respectively, and the simulations of Christensen et al. (2018). The left panel shows that the stellar metal mass fractions increase with M_* as a result of the stellar mass–metallicity relation. However, the simulated ISM metal mass fractions do not strongly correlate with M_* despite spanning

[11] Assuming that these "CGM/Outflow" and "CGM/Inflow" absorbers have similar properties as those "CGM" absorbers, we estimated their potential impact parameters by matching their log N values to the nearest "CGM" log N values with known impact parameters. We then included these absorbers in Equation (1) and found that they contributed a few thousand $M_\odot$, which is much less than the significant figure we adopted for the total estimated mass.

[12] $12 + \log({\rm Si/H})_{\rm IC1613} = 12 + \log({\rm O/H})_{\rm IC1613} + \log({\rm Si/O})_\odot$, where $\log({\rm Si/O})_\odot = \log({\rm Si/H})_\odot - \log({\rm O/H})_\odot$; we assume the ISM of IC 1613 has the same element composition as the Sun and adopt $12 + \log({\rm Si/H})_\odot = 7.51 \pm 0.03$ and $12 + \log({\rm O/H})_\odot = 8.69 \pm 0.05$ from Asplund et al. (2009) and $12 + \log({\rm O/H})_{\rm IC1613} = 7.73 \pm 0.04$ from Bresolin et al. (2007).

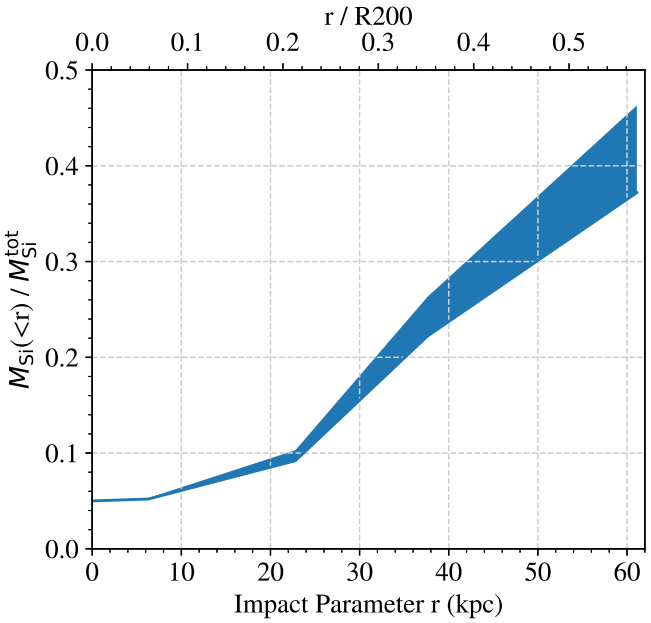

Figure 5. The cumulative mass fraction of Si in IC 1613 as a function of impact parameter. At each r, the cumulative value is computed by summing up the $M_{\rm Si}/M_{\rm Si}^{\rm tot}$ values at $\leqslant r$ in Table 4. The boundaries of the shaded blue region represent the lower and upper bounds of the mass fractions based on the $M_{\rm Si}$ values in Table 4.

four orders of magnitude in M_*. We suspect that even though these simulated galaxies follow a similar gas-phase mass–metallicity relation to their observational counterparts, the gas fractions in the galaxies decrease with M_* (El-Badry et al. 2018), resulting in the noncorrection in the ISM panel.

When compared to observations, the fraction of metals locked in the stars and ISM in all simulations are a factor of ∼2 or more higher than observed in IC 1613 and WLM. For instance, only 2%–6% of the Si are in the ISM of IC 1613 and WLM, as compared to ∼2%–60% of the metals contained in the simulated ISM. The discrepancy is likely to be due to (1) different definitions of the ISM, (2) different assumptions on stellar yields and stellar evolution modeling, and (3) the specific simulation setup and feedback treatment that expels metals from galaxies to various degrees. For (1), both Muratov et al. (2017) and Hafen et al. (2019) define the ISM as all gas within 0.1 virial radii. For a galaxy such as IC 1613, defining the ISM as within $0.1R_{200}$ would include gas within 10 kpc. However, the half-light radius of IC 1613 is only 1.5 kpc (McConnachie 2012) and the H I in its ISM extends to a radius of ∼2.5 kpc at a column density level[13] of 5×10^{19} cm^{-2}. Therefore, Muratov et al.'s (2017) and Hafen et al.'s (2019) ISM definition extends the ISM size by a factor of ∼4 and includes gas at higher temperatures that are typically not probed by H I 21 cm emission. Indeed, redefining the ISM as gas within 2.5 kpc for all FIRE galaxies in this stellar mass range does lower the average ISM metal mass fraction from ∼0.24 to ∼0.13 (FIRE, private communication, 2020). Christensen et al. (2018) defines the ISM as all gas with number density >0.1 cm^{-3}, temperature $<1.2 \times 10^4$ K, and within a cylindrical height of 3 kpc from the plane of the disk of their galaxies, which is more comparable for the particular properties of IC 1613. Even so, our measurements are still low compared to the typical simulated values. Note that the ISM definition would not change the values for the stellar metal fraction, which is similarly low for our observational estimates compared to what is expected from these simulations.

For (2), there are significant variations in the expected yield of Si depending on the choices of both nucleosynthetic yields and initial mass function (IMF). While this does not affect the results from the simulations as plotted because they are properly normalized by the total metals present in the computational domain, it does affect our observational estimates of the total amount of Si present. To understand the impact of this uncertainty, we bracket our observational estimates of WLM's and IC 1613's metal fractions in Figure 6 with the lower bounds estimated with $y_{\rm Si} = 1.64 \times 10^{-3}$ as adopted in the FIRE simulations and the upper bounds with $y_{\rm Si} \sim 3.7 \times 10^{-3}$ from Christensen et al. (2018) for their choice of stellar yields and IMF. Note that, in our estimates, we use $y_{\rm Si} = 3 \times 10^{-3}$ as discussed in Section 5.1. Figure 6 shows that varying $y_{\rm Si}$ values does result in a large range in the metal mass fraction in stars, ISM, and CGM, but the stellar and ISM values are still at the lower end of the prediction from simulated galaxies.

For (3), it is interesting that all simulations give broadly similar results in spite of their varying simulation setups and feedback recipes. It is beyond the scope of this work to explore deeply what sets the scatters in the simulations, but we note that among all the simulated galaxies there are some with similarly low metal fractions as IC 1613 and WLM. Therefore, it would be valuable to develop a larger observational sample of these types of measurements for a more statistically meaningful comparison across simulations.

Lastly, in the CGM panel, we find that IC 1613 and WLM contain as many metals as the simulations have predicted. No strong correlation is seen between the CGM metal mass fraction and M_*. Unlike the ISM, neither the gas-phase mass–metallicity relationship nor the gas mass fraction of the CGM is well studied observationally. Relevant CGM properties in the simulated galaxies also await further investigation in order to fully understand the scatters and the noncorrelation of the CGM metal fraction with M_*.

5.3. Metal Outflow Rate and Instantaneous Metal Mass Loading Factor

A number of "CGM/Outflow" absorbers are detected toward stellar sight lines S1–S4 (see Section 3). Because these sight lines were observed in a down-the-barrel manner, the impact parameters of these absorbers from the galaxy are unknown, which means they could be absorbers in the CGM or outflows in the immediate region of the galaxy. Similar distance ambiguity in identifying absorbers' distances relative to host galaxies has also troubled other down-the-barrel studies of gas flows in extragalactic systems (e.g., Rubin et al. 2012, 2014; Chisholm et al. 2016; Zheng et al. 2017). Hereafter, we assume that these absorbers probe outflowing material from IC 1613 and estimate the metal outflow rate $\dot{M}_{\rm out,Z}$ and instantaneous metal mass loading factor η_Z. Following the definition in

[13] To derive the H I extent of IC 1613's ISM, we analyze the VLA's natural-weighted map cube of IC 1613 from the LITTLE THINGS survey (Hunter et al. 2012). We generate a H I column density map of the galaxy by integrating the data cube from $v_{\rm LSR} = -360$ km s^{-1} to -120 km s^{-1} to include H I emission within ±120 km s^{-1} of the systemic velocity of IC 1613. We then smooth the column density map with Gaussian kernels and determine the extent of the H I by estimating the size of the column density contour at 5×10^{19} cm^{-2} over a velocity window of 240 km s^{-1}, which corresponds to the rms value as listed in their Table 3.

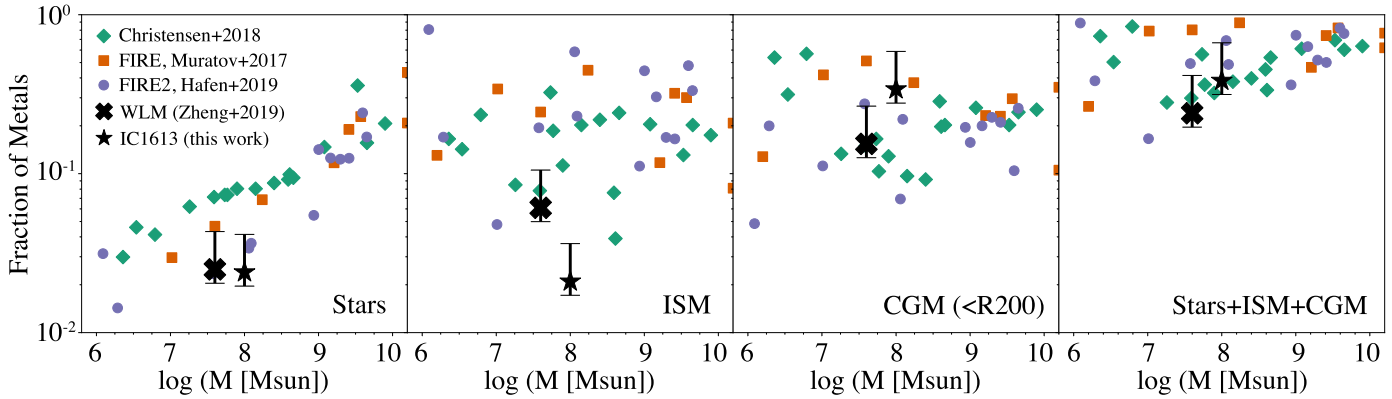

Figure 6. The mass fraction of metals in the stars, ISM, CGM, and their sum as a function of galaxy stellar mass for WLM (Zheng et al. 2019b), IC 1613 (this work), and a selection of recent suites of zoom-in simulations of individual, isolated galaxies from FIRE (Muratov et al. 2017), FIRE2 (Hafen et al. 2019), and Christensen et al. (2018). The error bars on the observational data points reflect only the potential variation in these quantities with the choice of stellar yield in Si between models. We emphasize that the definition of ISM and CGM between simulations and these observations differs. See Section 5.2 for more details. For IC 1613, the CGM value is computed only for gas within $0.6R_{200}$ as probed by our COS data.

Christensen et al. (2018), $\eta_Z \equiv \dot{M}_{\rm out,Z}/\dot{M}$ is the ratio of metal mass carried by outflows per unit time to the star formation rate at the present day. Note that η_Z is different from the effective metal mass loading factor or the instantaneous/effective gas mass loading factor that have been used in the literature.[14]

Given that S1–S4 are located at different corners of IC 1613 (see Figure 1), we assume a cylindrical geometry to represent the outflowing material with a radius of $R_{\rm out} = 2.5$ kpc based on the H I extent of the galaxy as calculated in Section 5.2 and footnote (See Footnote 12). The metal outflow rate $\dot{M}_{\rm out,Z}$ for an ion X can be derived as follows:

$$\begin{aligned}\dot{M}_{\rm out,Z} &= dM_{\rm out}/d{\rm t} = d(C_f \rho_x \pi R_{\rm out}^2 v_{\rm out} t)/d{\rm t} \\ &= mC_f \pi R_{\rm out}^2 v_{\rm out} m_x N_x / D_{\rm out}. \end{aligned} \quad (2)$$

In the equation, m_X and $N_{\rm X}$ are the atom mass and column density of ion X. $C_{\rm f}$ is the covering fraction, and we assume $C_{\rm f} = 1$ as the outflow absorbers are commonly detected among the stellar sight lines. $v_{\rm out}$ is the outflow velocity corrected for the galaxy's inclination, with typical values summarized in Section 3. $D_{\rm out}$ is the distance the outflows have reached. We adopt $D_{\rm out} = 1$ kpc (or $\sim 0.01R_{200}$) for two considerations. First, in order to derive the instantaneous $\dot{M}_{\rm out,Z}$ and η_Z values, we assume the outflows to have been enriching the vicinity of the galaxy within the past ~10–20 Myr at current outflow velocities. This is reasonable given that IC 1613 has a nearly continuous and constant star formation rate over the past >10 Gyr (Cole et al. 1999; Skillman et al. 2003, 2014; Weisz et al. 2014). Second, because $\rho_{\rm x} \equiv {\rm m_x} N_{\rm x}/D_{\rm out}$, not only does $D_{\rm out}$ represent the distance the outflows have reached, it also indicates the physical size of an outflowing ion absorber. Though we do not have information on the typical absorber size in IC 1613's CGM, a diameter of ~1 kpc is typically seen from observations of CGM absorbers of $L \geqslant 0.1L^*$ galaxies (Stocke et al. 2013; Werk et al. 2014). We find that the instantaneous outflow rate is $\dot{M}_{\rm out,Z} = 1.1 \times 10^{-5}\, M_\odot\, {\rm yr}^{-1}$ combining the measurements from Si II and Si III outflow-like absorbers. The total star formation rate of IC 1613 is $\dot{M} = 2.5 \times 10^{-3}\, M_\odot {\rm yr}^{-1}$ as measured from the Hα luminosity (Hunter & Elmegreen 2004). Therefore, the instantaneous metal mass loading factor is $\eta_Z = \dot{M}_{\rm out,Z}/\dot{M} = 0.004$ for Si II and Si III.

We do not use the Si IV lines because there are no robust Voigt-profile fits for these lines to effectively separate the ISM absorption from that of the outflows (Section 2.2). Instead, we run a grid of Cloudy models (Ferland et al. 2017) to estimate the Si IV column density based on the measurements of Si II and Si III, with the assumption that Si II, Si III, and Si IV are in the same phase. We implement an extragalactic UV background (Haardt & Madau 2001) and add ionizing flux from the star formation in the galaxy as a function of impact parameter and escape fraction as in Werk et al. (2014) as radiation sources. We find our results are not sensitive to the details of the ionizing background, but only its overall shape. We examine the results at a metallicty of 0.1 solar (Bresolin et al. 2007), a star formation rate of $2.5 \times 10^{-3}\, M_\odot\, {\rm yr}^{-1}$ (Hunter & Elmegreen 2004), and an escape fraction of 10%. At $N({\rm H\,I}) \leqslant 1.5 \times 10^{19}$ cm^{-2} for a line 30 km s^{-1} wide as measured from the VLA data (see Section 2.3), the constraint from the Si III/Si II ion ratio yields a nearly constant ionization parameter $\log U \sim (-3.3, -3.8)$ and a Si IV column density $N_{\rm SiIV} \sim 10^{10.9-11.7}$ cm^{-2} that is well below the detection limit of our COS spectra. Therefore, there is only a negligible amount of Si IV in the same phase as Si II and Si III in IC 1613's outflows. However, we cannot rule out the case that outflow-like Si IV absorbers are present in a warmer phase given that C IV is detected at $v_{\rm IC\ 1613} < -20$ km s^{-1} along some of the stellar sight lines. The lower ionization states of carbon and silicon offer no constraints on the warmer-phase material, and the predicted C IV/Si IV ion ratio depends strongly on the warm-phase N(H I), metallicity, and ionization state, none of which are known.

Without accurate N(Si IV) values, the metal outflow rate ($\dot{M}_{\rm out,Z} = 1.1 \times 10^{-5}\, M_\odot\, {\rm yr}^{-1}$) and the instantaneous metal mass loading factor ($\eta_Z = 0.004$) are deemed lower limits. When compared with simulations of dwarf galaxies, Christensen et al. (2018) find $\eta_z \sim 0.004$–0.01 at a circular velocity of $v_c = 40$ km s^{-1}, appropriate for a galaxy at the mass of IC

[14] The effective metal mass loading factor is a cumulative quantity of η_Z integrated over time; it is the ratio of the total metal mass a galaxy has lost throughout its star formation history to the total stellar mass ever formed. The instantaneous/effective gas mass loading factors are defined similarly, but with the nominator values from outflowing gas mass instead of metal mass (e.g., Christensen et al. 2016; Muratov et al. 2017).

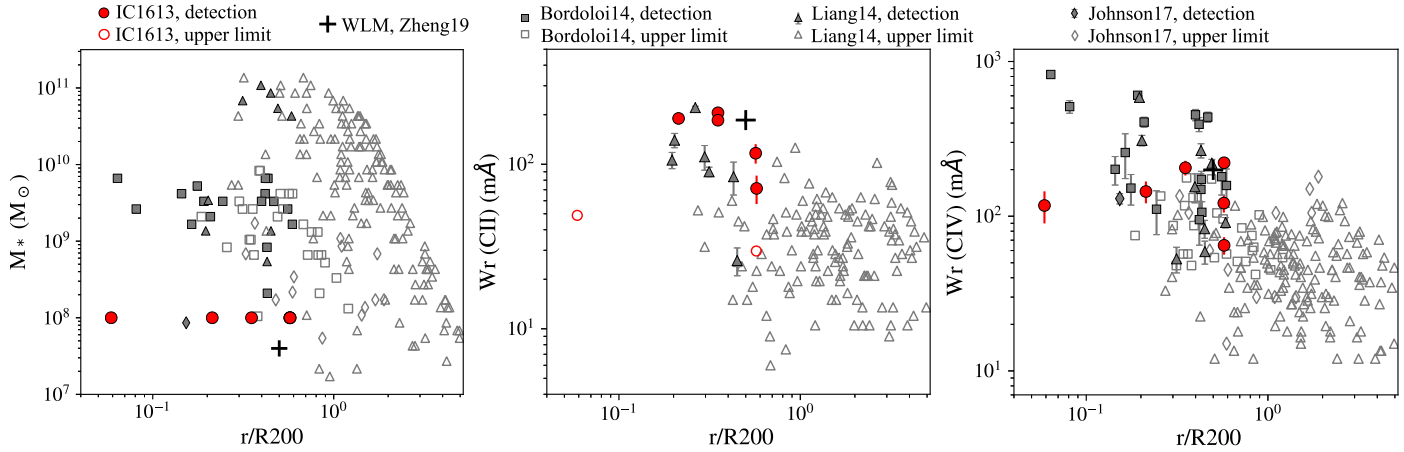

Figure 7. Left: host galaxy stellar mass (M_*) vs. impact parameter (r/R_{200}) for C IV absorbers from Bordoloi14, Liang14, Johnson17, Zheng19, and IC 1613 (this work). We show that IC 1613 and WLM probe a unique parameter space with low M_* and small r that has not been well studied before. Note that Liang14's sample also includes 8 sight lines near host galaxies with $M_* < 10^7\,M_\odot$ or at $r/R_{200} > 5$ that we do not show in this figure, and all of them are nondetections. Middle and right panels: equivalent width (W_r) as a function of impact parameter scaled with R_{200}. We choose to use W_r values instead of $\log N$ because it is the most common measurement among the three low-z dwarf studies. For IC 1613, we only use those measurements tagged as "CGM" or "Non-Detection" toward Q1–Q6. For absorbers from Bordoloi14, Liang14, Johnson17, and Zheng19, solid symbols show detection, and open ones indicate 3σ upper limits for nondetection.

1613 (see also Muratov et al. 2017). Though there have been constraints for dwarf galaxies' outflow gas mass loading factors (McQuinn et al. 2019), metal mass loading factors are rarely observationally determined. McQuinn et al. (2019) show that the gas mass loading factors range from 0.2 to 7 for a sample of nearby low-mass galaxies ($M_* \sim 10^{7\text{–}9.3}\,M_\odot$) based on H$\alpha$ emission-line observations; however, as they noted, the gas mass loading factors and the metal mass loading factors are not directly comparable without the knowledge of the phases of the outflowing metals.

Lastly, we highlight that $\eta_Z \geqslant 0.004$ is consistent with the stellar yield y_{Si} (=0.003) adopted in Section 5 despite them being derived under different sets of assumptions for IC 1613. For every unit of star formed, a fraction of $\geqslant$0.004 of the stellar mass is in the form of metal (Si) outflows. Furthermore, assuming a constant outflow rate over the lifetime of the galaxy ($T \sim 14$ Gyr) given its constant star formation history (Skillman et al. 2014), the total amount of Si accumulated in the CGM would be $\dot{M}_{\rm out,Z}\,T \geqslant 1.5 \times 10^5\,M_\odot$. This is consistent with the Si mass in the CGM from Section 5.1 that we derive based on Si II, Si III, and Si IV column density measurements along the Q1–Q6 sight lines.

6. Discussion

6.1. The CGM of Other Low-mass Galaxies

We first compare our ion absorbers near IC 1613 with those measured in and near the CGM of low-z dwarf galaxies studied by Bordoloi et al. (2014, hereafter Bordoloi14), Liang & Chen (2014, hereafter Liang14), and Johnson et al. (2017, hereafter Johnson17), and a dwarf irregular galaxy WLM in the LG (Zheng19). Because different IMFs were used to derive the stellar mass (M_*) in different studies, we convert their M_* values from the corresponding IMF (i.e., Salpeter 1955; Chabrier 2003) to that of Kroupa (2001). This is to be consistent with the IMF choice in our adopted M_*–M_h relation from Moster et al. (2010; see Section 2). Specifically, using the rescaling factors recommended in Madau & Dickinson (2014), we multiply the M_* values from Bordoloi14 by 0.66 to convert from the Salpeter IMF to the Kroupa IMF. We multiply the M_* values from Liang14 and Johnson17 by 1.08 to convert from the Chabrier IMF to the Kroupa IMF.

In the left panel of Figure 7, we show the range of galaxy stellar mass M_* and impact parameter r covered by these studies, and highlight that the sight lines near IC 1613 and WLM probe a unique parameter space at $M_* \lesssim 10^8\,M_\odot$ and $r \lesssim 0.6R_{200}$ that has not been well studied before. Bordoloi14 studied C IV absorption in the CGM of 43 low-mass galaxies at $z \leqslant 0.1$; their sample probes the inner CGM from $0.05R_{200}$ to $0.5R_{200}$, but focus on more massive galaxies with $M_* \sim 10^{8.2\text{–}10.2}\,M_\odot$. Liang14 studied Ly$\alpha$, C II, C IV, Si II, Si III, and Si IV absorbers within 500 kpc of 195 isolated galaxies at $z < 0.176$. Their sample includes a wide range of galaxy stellar masses with $M_* \sim 10^{5.2\text{–}11.1}\,M_\odot$, but 90% of the sight lines are at $>0.6\,R_{200}$ and do not have detection. Johnson17 studied 18 star-forming field dwarfs with $M_* \sim 10^{7.7\text{–}9.2}\,M_\odot$ and $r/R_{200} \sim 0.2$–2; while most of their sight lines find a nondetection of metal lines, the one at $M_* = 10^{7.9}\,M_\odot$ and $r = 0.15R_{200}$ shows Si III and C IV absorbers with similar equivalent widths to those near IC 1613 and WLM.

In the middle and right panels of Figure 7, we show the W_r values of C II and C IV as a function of impact parameter scaled with R_{200}. For consistency, we recalculate R_{200} for all galaxy halos from Bordoloi14, Liang14, Johnson17, and Zheng19 using our R_{200} definition as detailed in Section 1. This definition is consistent with what is used by Bordoloi14 and Zheng19, but systematically larger than those adopted by Liang14 and Johnson17. The latter defines R_{200} based on the critical density with an overdensity factor Δ_c from Bryan & Norman (1998). Figure 7 shows that detection mainly occurs within $0.6R_{200}$ and the W_r values of the detected absorbers are consistent among various works. Results of Si III and Si IV are similar. Bordoloi14 found a power-law decline in C IV's equivalent widths out to $\sim 0.5R_{200}$; we do not observe such a trend in C IV detected near IC 1613 , likely due to the

sparse data points in our sample. Regarding the total metal content, we find that the LG dwarf galaxies ($M_* \sim 10^{7-8}\,M_\odot$) host a reservoir of metals with mass similar to those low-mass galaxies at low redshifts.

In the LG, thus far there have been limited studies of the CGM of dwarf galaxies. Zheng et al. (2019b) reported a tentative detection of CGM absorber at $0.5R_{200}$ in WLM (Figure 7). The uncertainty in their diagnosis of the absorber's origin is also due to the chance alignment with the foreground Magellanic System in the $L_{\rm MS}$–$v_{\rm LSR}$ diagram, as shown in Figure 4. Our investigation that the $L_{\rm MS}$–$v_{\rm LSR}$ diagram does not yield a robust diagnosis on an absorber's connection to the Magellanic System (see Section 4) now has provided a stronger argument for the absorber's association with WLM's CGM. The Si mass derived for WLM's CGM is $\sim$(0.2–1.0) $\times$ $10^5\,M_\odot$, which is similar to what we derive for IC 1613.

Furthermore, in a study of Milky Way's ionized high-velocity gas, Richter et al. (2017) also looked for metal absorption-line features along QSO sight lines within impact parameters of $\sim$0.5–2 virial radii of 19 LG dwarf galaxies with or without gas, but did not find significant detection near the systemic velocities of host galaxies. They concluded that there was no compelling evidence of CGM gas near LG dwarf galaxies. However, it is worth noting that the detectability of the CGM absorbers in their data could be compromised because of the low S/N criterion they adopted to choose the spectra (S/N $\geqslant$ 6) and the large impact parameters of the sight lines (>0.5 virial radius).

Though current observational effort of low-mass galaxies' CGM is limited, upcoming HST/COS programs, such as GO-16301 (PI Putman) and GO-15227 (PI Burchett), will provide a promising, large sample of nearby low-mass galaxies for statistically significant comparisons on CGM metal content.

6.2. The Metal Content in Other LG Dwarf Galaxies

Our estimate of the Si mass fraction locked in the stars of IC 1613 ($\sim$3%) is consistent with what has been measured for some other LG dwarf galaxies. Kirby et al. (2011, 2013) show that $\geqslant$96% of the iron ever produced in LG dwarf galaxies is no longer locked in their stars. In addition to WLM, as we have compared with in Section 5.2, another interesting galaxy to discuss is Leo P. Discovered by Giovanelli et al. (2013), Leo P is also an isolated dwarf irregular galaxy that is far away from a massive host. Therefore, the galaxy is unlikely to lose its gas through stripping; instead, any gas lost was probably pushed out by stellar feedback. McQuinn et al. (2015a) find that the mass of oxygen retained in the stars and ISM of Leo P is 5%, same as IC 1613. Interestingly, Leo P has a stellar mass 180 times less than IC 1613 ($M_{*,\rm LeoP} = 5.6 \times 10^5\,M_\odot$; McQuinn et al. 2015b). The similar metal retention fractions of Leo P and IC 1613 challenge the correlation between the metal mass fraction in the stars and the M_* of the simulated galaxies as shown in the left panel of Figure 6. More simulations on dwarf galaxies at Leo P's mass (e.g., Rey et al. 2020) are needed to further investigate how the metal fractions in stars scale with M_* at much lower mass regime.

7. Conclusion

With four stellar and six QSO sight lines observed with HST/COS, we study the CGM and outflows of IC 1613, an isolated, low-mass ($M_* \sim 10^8\,M_\odot$) dwarf irregular galaxy on the outskirts of the LG. IC 1613 is among the lowest-mass galaxies ever studied in the context of CGM metal content and outflows, and it is one of the rare cases whose CGM is probed by more than one QSO sight line except for the Milky Way and M31.

Our stellar and QSO sight lines probe a wide range of impact parameters, from $<0.1R_{200}$ to $0.6R_{200}$, and detect a number of Si II, Si III, Si IV, C II, and C IV ion absorbers. We consider an absorber to be associated with IC 1613's CGM, ISM, outflow, or inflow if its velocity is within the escape velocity of the galaxy (thus gravitationally bound). When comparing the IC 1613-associated absorbers with those of dwarf galaxies at low z, we find that the absorbers near IC 1613 have similar line strengths.

We estimate a silicon mass of $M_{\rm Si}^{\rm CGM} \approx$ (1.0–1.3) $\times$ $10^5\,M_\odot$ within $0.6R_{200}$ of IC 1613's CGM, assuming that the majority of the Si is in the ionization states of Si II, Si III, and Si IV. We also estimate the Si metal content in the stars and ISM based on IC 1613's stellar mass, H I mass, theoretical nucleosynthetic yields, and gas-phase metallicity. We find $M_{\rm Si}^{*} \sim 8 \times 10^3\,M_\odot$ for Si locked in the stars and $M_{\rm Si}^{\rm ISM} \sim 7 \times 10^3\,M_\odot$ for Si in the ISM. Overall, of all the Si ever been produced in IC 1613, $\sim$3%, $\sim$2%, and $\sim$32%–42% of the mass is in the stars, ISM, and within $0.6R_{200}$ of the galaxy's CGM (see Figure 6), which accounts for nearly half of the total Si mass budget. The remaining $\sim$50%–60% of the Si mass is either in the outer CGM of IC 1613 ($0.6 < r/R_{200} < 1$) or has escaped beyond the virial radius of the galaxy. Our results are largely consistent with predicted values from existing simulations, although large scatters in the ISM and CGM metal fractions are found in simulated galaxies at different masses (see Figure 6).

Lastly, based on the Si II and Si III measurements of the outflow-like absorbers toward S1–S4, we find a metal outflow rate of $\dot{M}_{\rm out,Z} \geqslant 1.1 \times 10^{-5}\,M_\odot\,{\rm yr}^{-1}$ and an instantaneous metal mass loading factor of $\eta_{\rm z} \geqslant 0.004$, consistent with the predicted values for simulated galaxies at similar masses. We highlight that, assuming a constant metal outflow rate throughout IC 1613's star formation history, the total Si mass in the galaxy's CGM as enriched by these metal outflows is consistent with the current CGM mass independently measured from the QSO sight lines Q1–Q6.

To conclude, our work shows that there is a large mass reservoir of silicon in the CGM of IC 1613, which has been continuously enriched by metal outflows throughout the galaxy's star formation history. Our results are largely consistent with what has been predicted for simulated galaxies at similar masses. We are looking forward to compiling a larger observational sample consisting of nearby low-mass galaxies to yield a statistically meaningful assessment on how the CGM and metal outflow properties vary from galaxy to galaxy and from observations to simulations.

We thank R. Bordoloi for sharing his python code of escape velocity calculation, E. Patel for discussing the projection effect between the Magellanic System and the LG galaxies using hydrodynamic simulations and HST/Gaia proper motion measurements, and D. Weisz for discussing many aspects of this paper and for his great support as a faculty mentor to Y.Z. at Miller Institute at UC Berkeley. We also thank A. Fox and P. Richter for helpful discussion on the manuscript. Y.Z.

acknowledges support from the Miller Institute for Basic Research in Science. Support for Program number HST-GO-15156 was provided by NASA through a grant from the Space Telescope Science Institute, which is operated by the Association of Universities for Research in Astronomy, Incorporated, under NASA contract NAS5-26555. This material is based upon work supported by the National Science Foundation under grant No. AST-1847909. E.N.K. gratefully acknowledges support from a Cottrell Scholar award administered by the Research Corporation for Science Advancement. This research has made use of the HSLA database, developed and maintained at STScI, Baltimore, USA.

Facilities: Hubble Space Telescope/Cosmic Origins Spectrograph, Mikulski Archive for Space Telescopes (MAST).

Software: Astropy (The Astropy Collaboration et al. 2018), Numpy (Harris et al. 2020), Matplotlib (Hunter 2007), CLOUDY (Ferland et al. 2017), IDL, the gala package (Price-Whelan et al. 2017).

Appendix A
Spectral Coaddition

Spectra observed with HST/COS are processed by the standard CalCOS pipeline up to visit level; however, those taken with different grating setups remain separate. Wakker et al. (2015) point out that the CalCOS pipeline often overestimates the errors of coadded spectra for faint targets with fluxes $\lesssim 10^{-14}$ erg cm^{-2} s^{-1} Å^{-1}. A number of authors have written their own coadding codes (e.g., Danforth et al. 2010; Keeney et al. 2012; Tumlinson et al. 2013; Wakker et al. 2015). To produce science-ready coadded spectra in our work, here we focus on two publicly available resources, the HSLA and coadd_x1d (Danforth et al. 2010; Keeney et al. 2012). We describe how they work and compare the spectral coaddition products.

The second data release of the HSLA publishes coadded spectra for targets observed with HST/COS that went public as of April 2017. In their algorithm, multiexposure spectra were coadded using photon counts from each file (Gehrels 1986), and then the total counts were converted to flux density based on the flux calibration ratio from the keyword FLUXFACTOR recorded in the original fits file header. Flux errors were handled using Poisson statistics. Because of the large data volume and the diverse target types of the HST/COS database, HSLA did not perform wavelength calibration and instead adopted the original wavelengths provided by the CalCOS pipeline for each file. This may result in artificial line profiles if spectra from different exposures had systemic velocity shifts.

Meanwhile, the coadd_x1d code (Danforth et al. 2010; Keeney et al. 2012) chooses to coadd multiexposure spectra based on fluxes instead of photon counts. Users running the code can decide among three different weighting options to coadd spectra: (1) exposure time, (2) inverse variance, or (3) the square of S/N per exposure. As pointed out by Wakker et al. (2015), the inverse-variance weighting in option (2) may give rise to potential line-shape distortion if different data files are observed with different exposure times. Similar to the HSLA, the coadd_x1d also handles error arrays based on Poisson statistics. For wavelength calibration, the coadd_x1d derives constant velocity shifts using a number of strong interstellar lines over 10 Å windows among all input exposures. Then, it manually applies the velocity shifts to all exposures to align their wavelengths with a randomly selected reference exposure. As noted by Zheng et al. (2017), such an alignment procedure may introduce a velocity offset of $\sim$10 km s^{-1}, which is smaller than the COS wavelength accuracy of 15–20 km s^{-1} (see the COS Instrument Handbook).

We run the coadd_x1d code to process the spectra for all the targets using the three weighting options mentioned above and compare the difference in terms of the flux levels. Moreover, for 5 of the 10 targets, S3, S4, Q4, Q5, Q6 that have coadded spectra from HSLA, we also compare the results between coadd_x1d and HSLA. We design two steps to evaluate the performance of the two coaddition routines:

1. We compare the coadded spectra with each of the original exposure files (i.e., **x1d.fits) to check if line profiles and fluxes are consistent after coaddition. For the G130M grating, we check two 15 Å wide spectral regions: [1248, 1263] Å for S II 1250/1259/1260 Å and [1390, 1405] Å for Si IV 1393/1402 Å. For G160M, we check another two 15 Å wide spectral regions: [1540, 1555] Å for C IV 1548/1550 Å and [1600, 1615] Å for Fe II 1608 Å. We only compare the flux levels because the errors of the coadded spectra will be reduced, and thus lower than those of each individual exposure file. We show a typical flux level comparison in Figure A1. Among all the targets we analyze, we find that all coadded spectra show visibly similar line profiles to each individual exposure; however, the flux levels differ depending on the method in use. Generally speaking, coadd_x1d with method 3 (2) often yield higher (lower) fluxes than those of individual exposures, with absolute flux offset larger than 10^{-16}–10^{-15} erg cm^{-2} s^{-1} Å^{-1}. coadd_x1d with method 1 and HSLA coadded spectra (when available) show consistent flux levels with individual exposures in most cases, with absolute flux offset less than $\lesssim 10^{-17}$ erg cm^{-2} s^{-1} Å^{-1}.
2. We further quantify the differences between HSLA and coadd_x1d coadded spectra by calculating flux ratios of coadd_x1d spectra to HSLA's at a number of absorption-line-free regions. This step is only applied to S3, S4, Q4, Q5, and Q6 because they were included in the recent HSLA coadded spectra release. In Figure A2, we show an example of the flux ratio comparison using the same target (S3) as in Figure A1. Overall, for S3, S4, and Q4, we find consistent fluxes between coadd_x1d with method 1 and HSLA, with flux ratios nearly 1.0. For Q5 and Q6, we find the flux ratios deviate from 1.0 by less than 15%. The spectra coadded with methods 2 and 3 show less consistent results with HSLA's, especially at longer wavelengths.

In all, we find that the line profiles are not significantly altered during the coadded procedures of HSLA or coadd_x1d. When comparing coadded flux levels, we find that HSLA and coadd_x1d with method 1 provide the most consistent coadded fluxes in comparison with the original individual exposure files. coadd_x1d with method 2 (3) often produce spectra with flux values that are too low (high) . Therefore, we decide to use the HSLA coadded spectra for our analyses when available (i.e., S3, S4, Q4, Q5, Q6). For targets without HSLA coadded spectra (i.e., S1, S2, Q1, Q2, Q3), we process the data using coadd_x1d with method 1. In Figures A3–A12, we show the

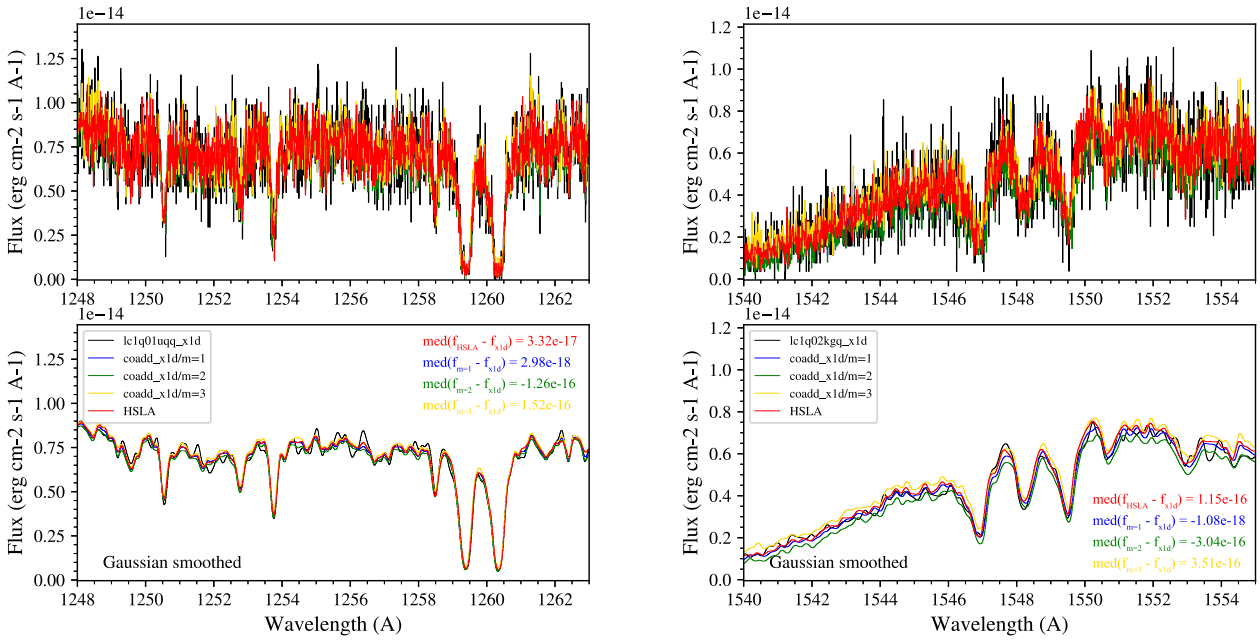

Figure A1. The flux level comparison among the HSLA (red), coadd_x1d (green, blue, gold), and the original individual exposure files (black) for S3, which is typical among all of the targets we analyzed. The top panels are for data without binning, and the bottom panels for data that are Gaussian smoothed to 6 pixels (i.e., per resolution element). The left and right panels show two different spectral regions. The indicated values show median flux offsets between a given method and one of the original x1d.fits exposure files. We generate similar figures for every exposure to check line profile and flux consistency. Overall, we find that the HSLA and coadd_x1d within method 1 show much better flux consistency with the original exposures, with a typical median flux offset $\lesssim 10^{-17}$ erg cm^{-2} s^{-1} Å^{-1}. Meanwhile, the coadd_x1d with method 2 (3) often gives too low (high) flux values, with absolute flux offset often higher than 10^{-16}–10^{-15} erg cm^{-2} s^{-1} Å^{-1}.

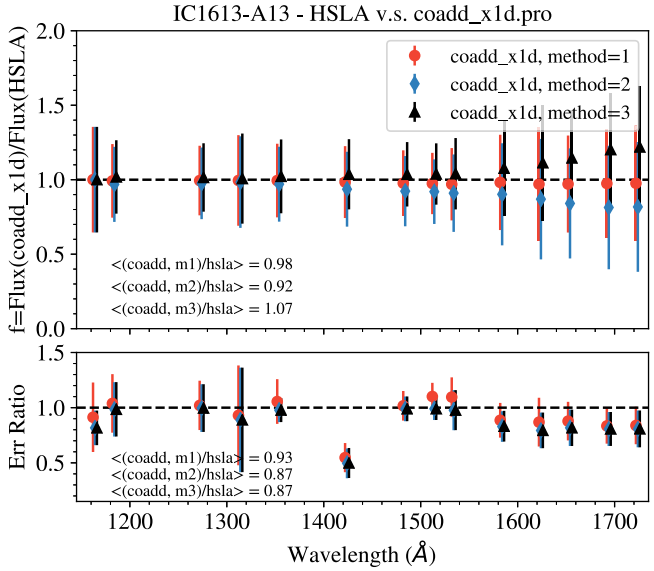

Figure A2. Flux ratios of absorption-free spectra from coadd_x1d methods 1 (red circle), 2 (blue diamond), and 3 (black triangle) to HSLA's at different wavelengths. At each wavelength, the flux ratio is sampled over a 10 Å spectral window. Ratio of 1.0 indicates consistent coadded spectral fluxes between a given coadd_x1d method and HSLA. Overall, coadd_x1d with method 1 yields much more consistent coadded spectral fluxes with HSLA than method 2 or 3.

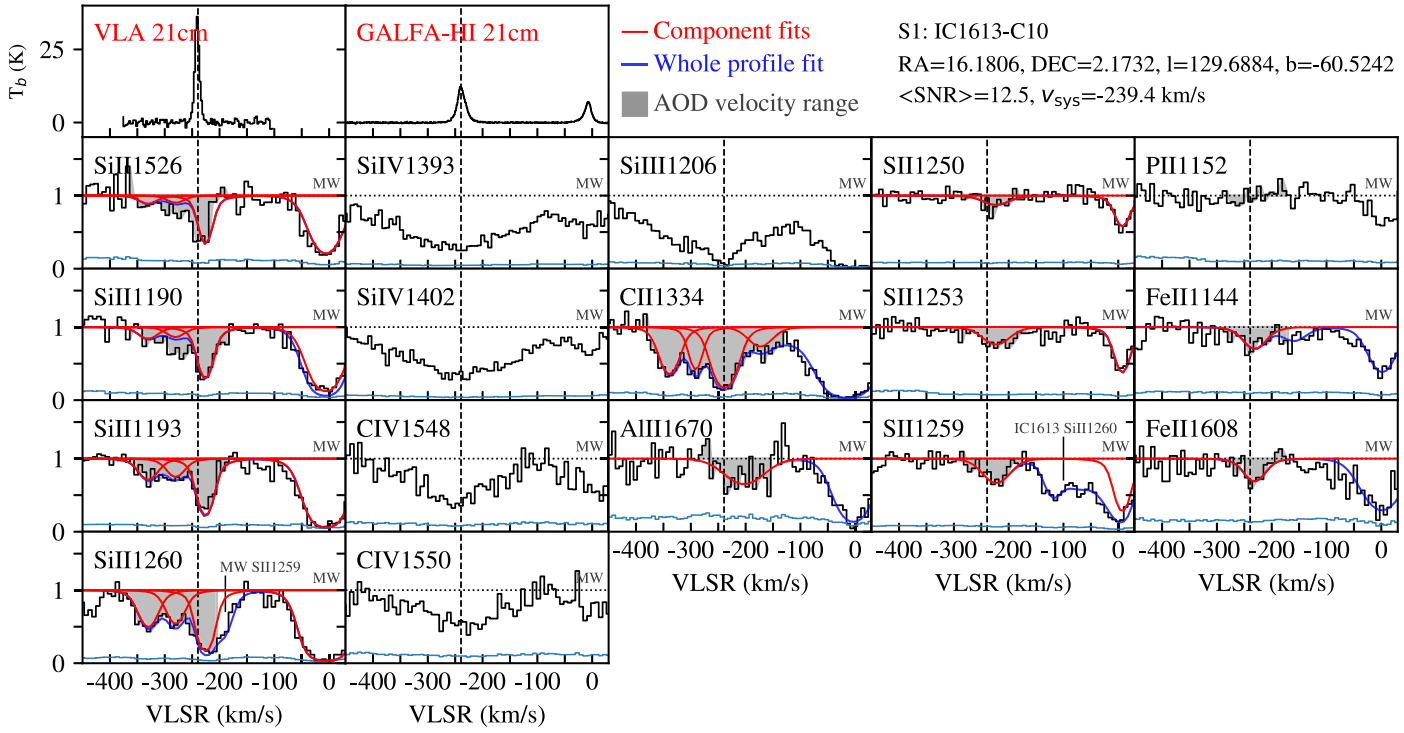

Figure A3. S1: IC 1613-C10. The top two panels show H I data from VLA (Hunter et al. 2012) and from the GALFA-H I DR2 (Peek et al. 2018). The rest of the panels show continuum-normalized ion lines and their Voigt-profile fits when available. The red curves are for individual component fits; the blue curves indicate the whole profile fits, which are the sum of the red curves and nuisance components (e.g., the Milky Way's ISM). The dashed line in each panel indicates the systemic velocity of IC 1613, v_{sys}. The Si III, Si IV, and C IV lines are broad without distinguishable individual components; we attempted Voigt-profile fitting for these lines, but could not find converging results with realistic component widths of $b \leqslant 50$ km s^{-1}. We decide not to use Si III, Si IV, and C IV lines in this case even though extended wind features can be seen in the line profiles.

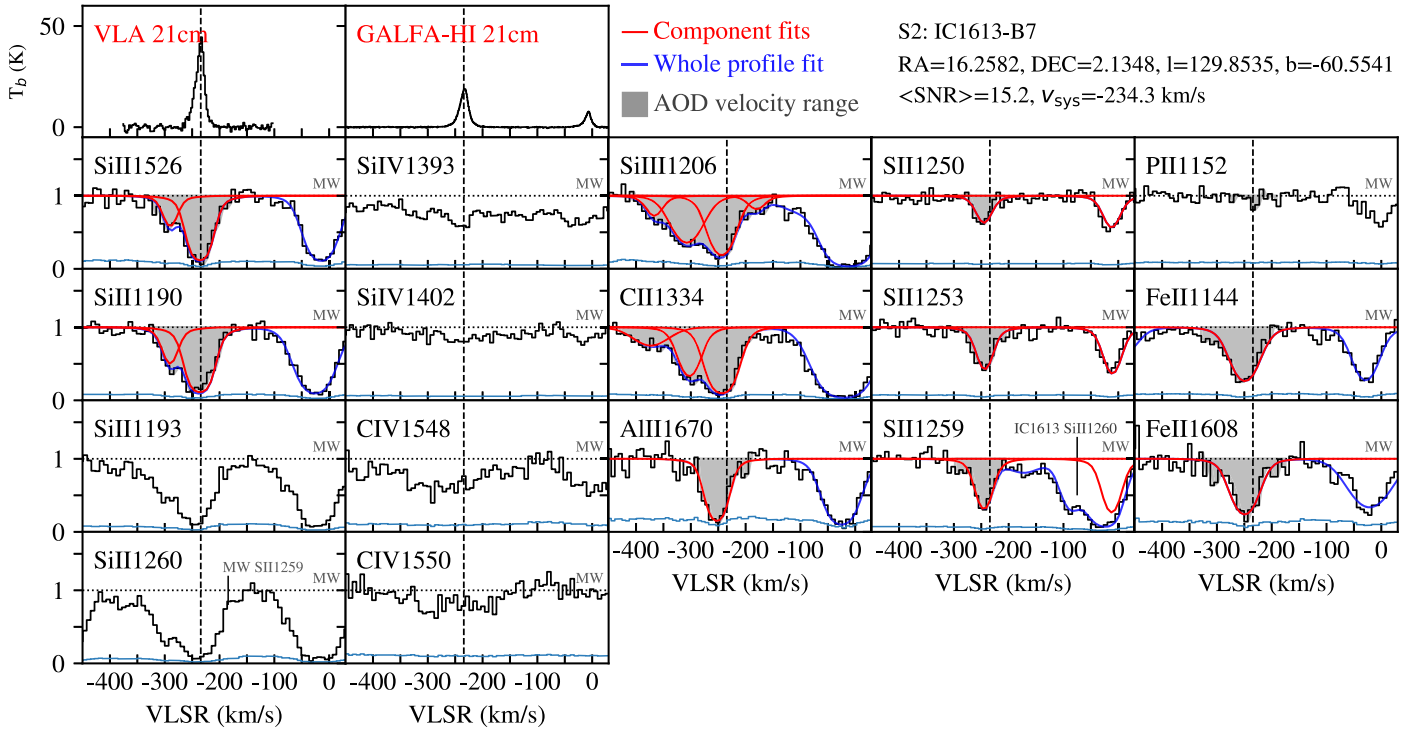

Figure A4. S2: IC 1613-B7. See Figure A3 for figure legend description. Even though there are detectable absorption features in the Si IV 1393/1402 and C IV 1548/1550 lines, we cannot find robust Voigt-profile fitting results for these lines. And because they are blended with ISM absorption from IC 1613 and there is no efficient way to separate the ISM and wind signals, we decide not to use these lines. In addition, we do not use Si II 1193 in our fitting because the line is heavily saturated. We do not use Si II 1260 either because of its high saturated and contamination from the Milky Way's S II 1259 lines.

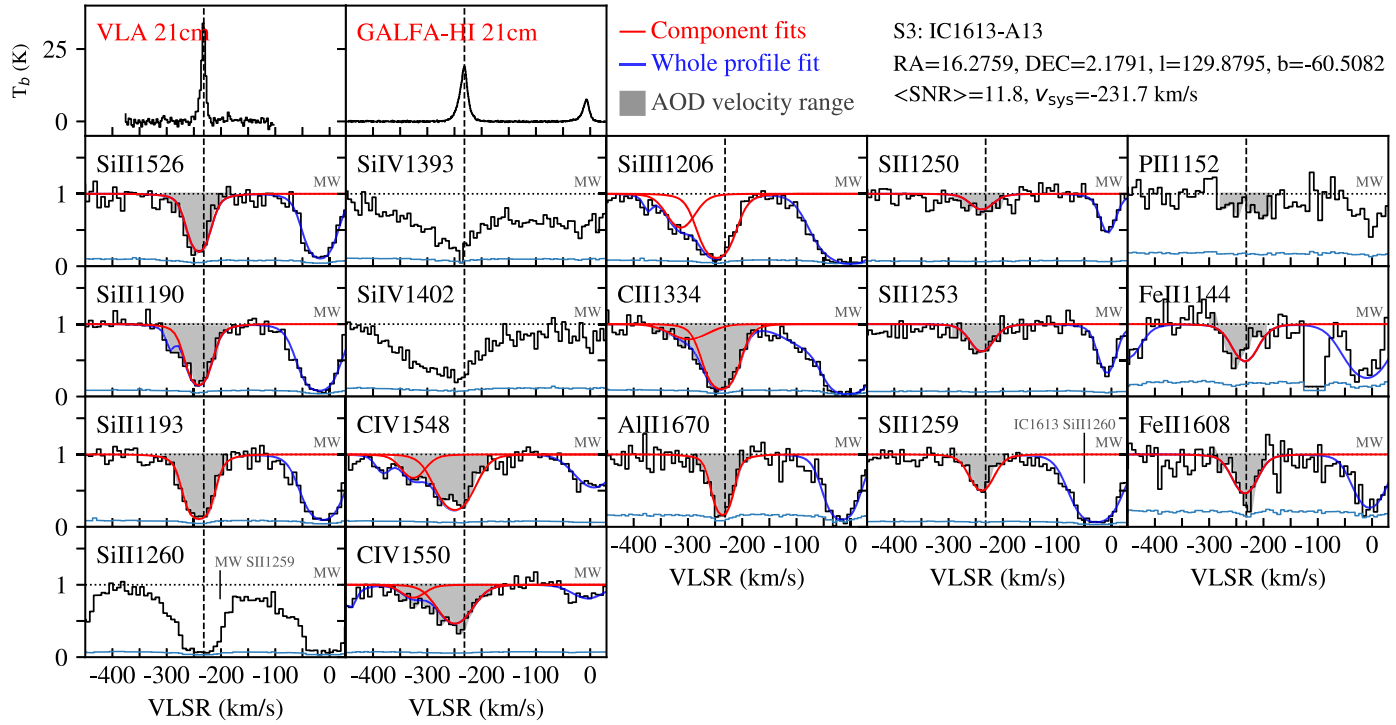

Figure A5. S3: IC 1613-A13. See Figure A3 for figure legend description. Most of the lines can be successfully fitted with Voigt profiles except the Si IV doublets, which appear to be broad without apparent individual line components. Meanwhile, Si IV 1402 Å is blended with an unknown feature which seems stronger than the corresponding part in Si IV 1393 Å.

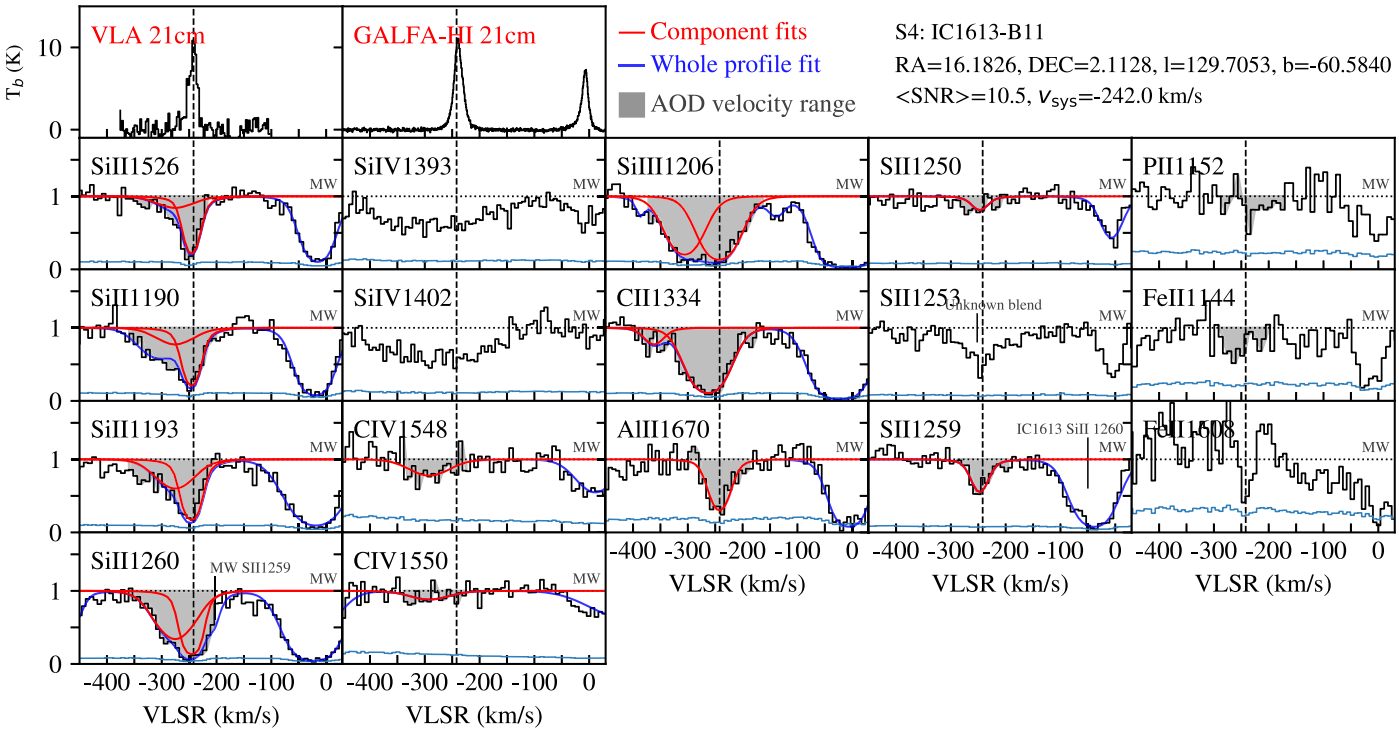

Figure A6. S4: IC 1613-B11. See Figure A3 for figure legend description. S II 1253 Å appears to be abnormally broader and stronger than S II 1250 Å and S II 1259 Å. Fe II 1608 Å is highly noisy and the Milky Way component of the line is likely to be contaminated by stellar lines. We do not find robust Voigt-profile fits for the Si IV 1393/1402 lines.

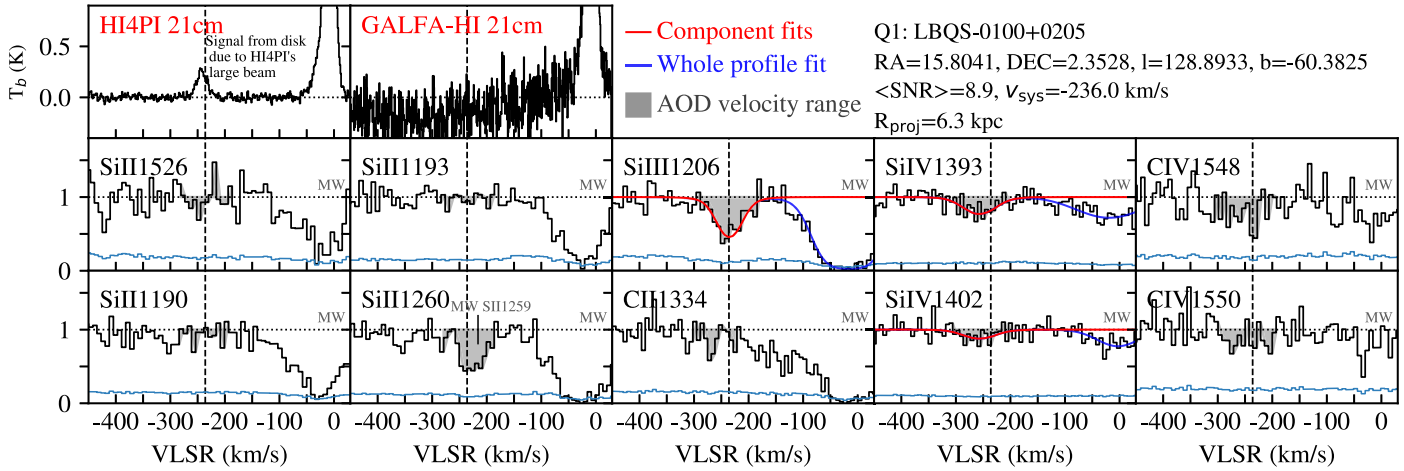

Figure A7. Q1: LBQS-0100+0205. See Figure A3 for figure legend description. The H I 21 cm signal in HI4PI is from the disk due to the large beam size (16′.2) of the data. For all of the QSO sight lines, v_{sys} is from the galaxy's systemic velocity determined from the H I 21 cm observation by Lake & Skillman (1989) and M12. C II 1334 Å is blended with the wing from the same line of the Milky Way's ISM, as well as C II* 1335. No detection in Si II 1526/1190/1193 Å. The absorption feature in the Si II 1260 Å line is in fact due to S II 1259 Å from the Milky Way's ISM. Unlike our stellar sight lines S1–S4, we do not study P II, Fe II, S II, and Al II along QSO sight lines Q1–Q6 because these ions are uncommon in a galaxy's CGM due to their low-ionization states.

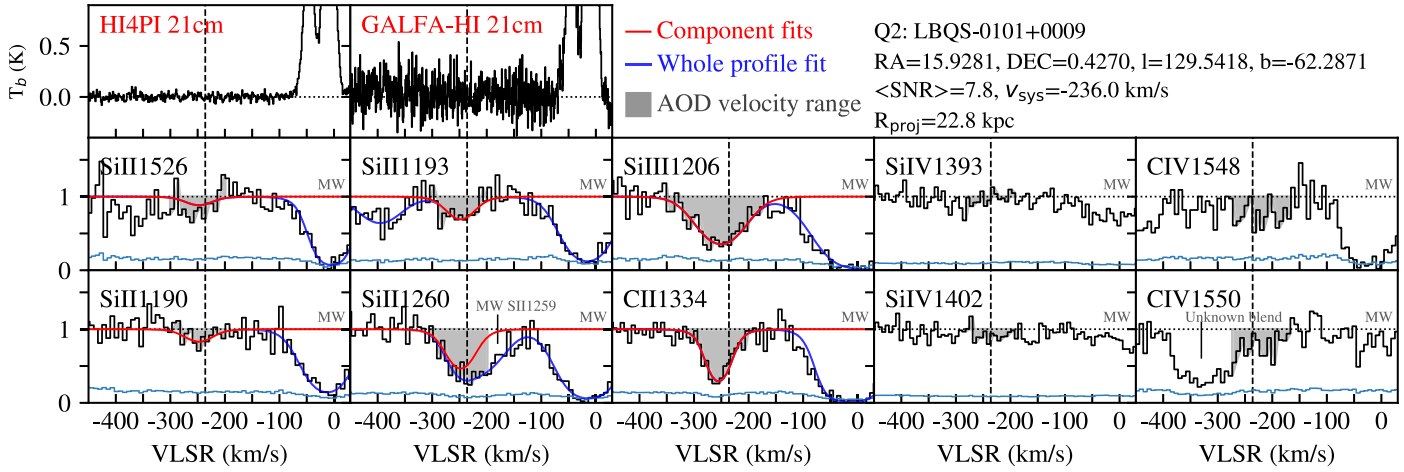

Figure A8. Q2: LBQS-0101+0009. See Figure A3 for figure legend description. The left wing of C IV 1550 Å is blended with a broad feature that cannot be identified.

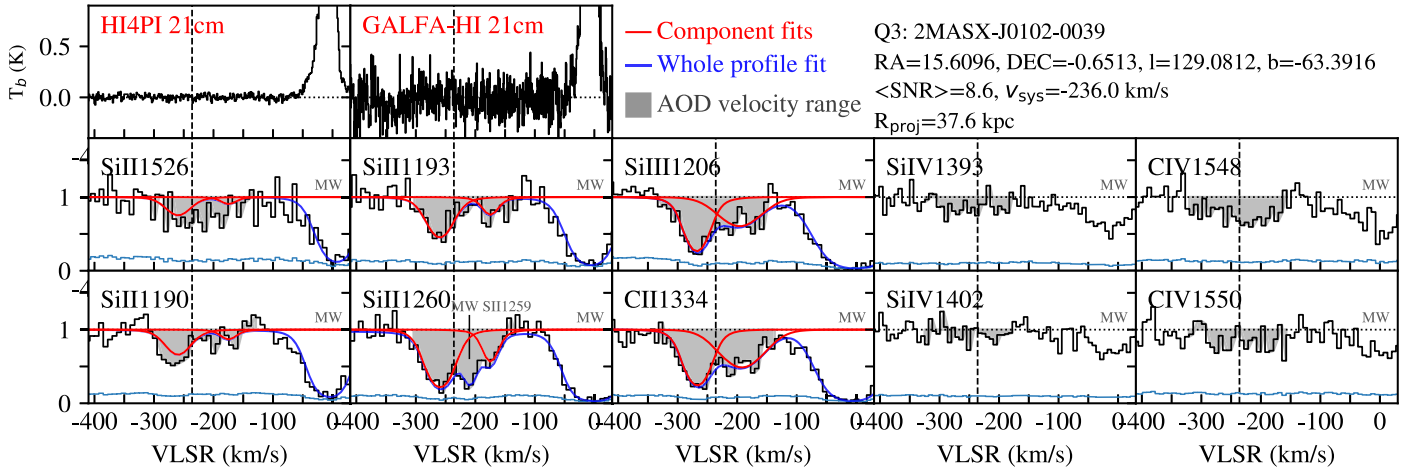

Figure A9. Q3: 2MASX-J0102-0039. See Figure A3 for figure legend description. No converging Voigt-profile solutions can be found in C IV doublets without invoking b values larger than 50 km s^{-1}.

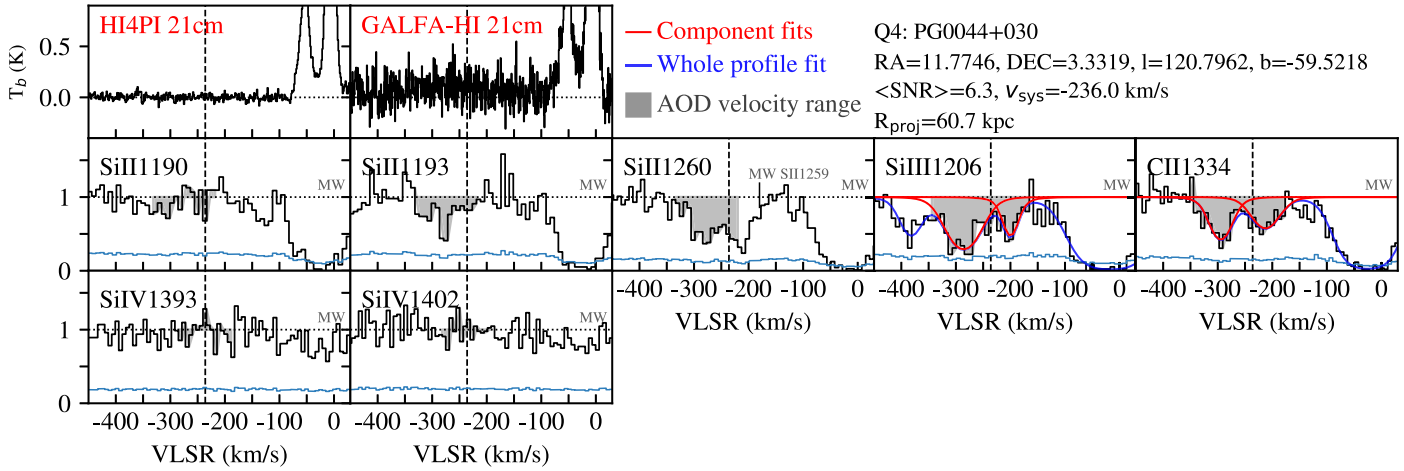

Figure A10. Q4: PG0044+030. See Figure A3 for figure legend description. This target only has G130M grating, so there are no data for Si II 1526 Å and C IV doublet.

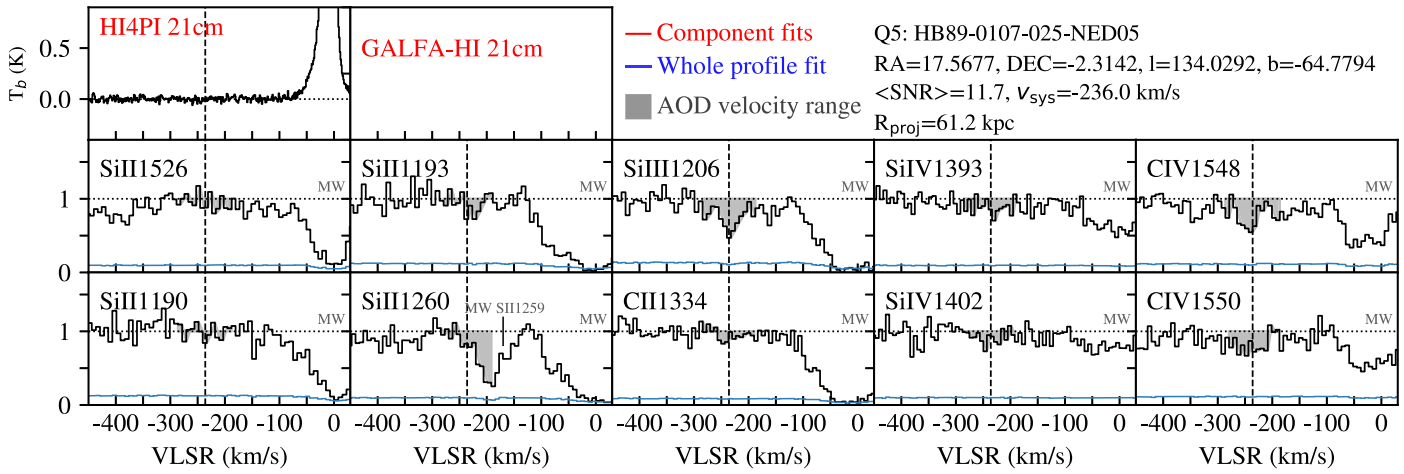

Figure A11. Q5: HB89-0107-025-NED05. See Figure A3 for figure legend description. Most of the lines do not have detection or 1σ–2σ absorption signals.

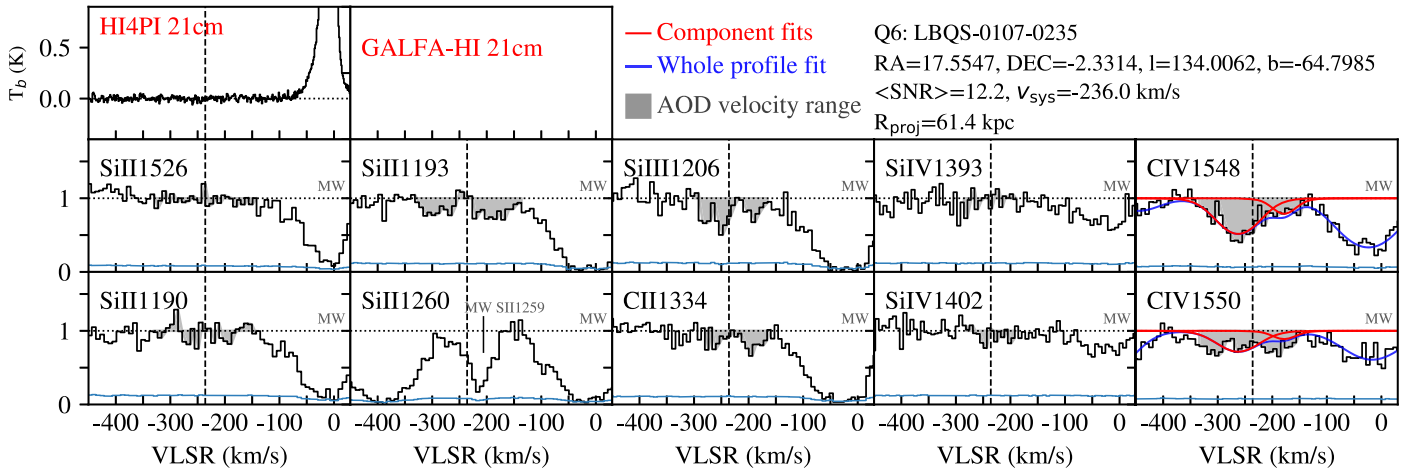

Figure A12. Q6: LBQS-0107-0235. See Figure A3 for figure legend description. C IV 1550 Å has a different line profile from its 1548 Å counterpart.

coadded spectral lines and their Voigt-profile fitting results for all of the targets.

Appendix B
Dwarf Galaxies' CGM Absorbers near the Magellanic System

In Section 4, we have shown that the LG galaxies at $d_\odot > 300$ kpc are coincidentally aligned with the H I emission from the Magellanic System on the position ($L_{\rm MS}$)—velocity ($v_{\rm LSR}$) diagram, with which we argue that the ionized cross section of the Magellanic System should be revisited using more robust methods other than the position–velocity diagram. Here we further show that potential CGM absorbers that originated from the H I-rich members of these LG galaxies would appear in a similar $L_{\rm MS}$–$v_{\rm LSR}$ parameter space, further complicating the diagnosis of an absorber's origin.

Among the 81 LG dwarf galaxies at $d_\odot > 300$ kpc as shown in Figure 4, we find 40 H I-rich galaxies (36 dwarfs and M31, M33, NGC 55, and NGC 300) that potentially have extended CGM that could be confused with the Magellanic ionized gas in projection. We show the angular extents of the dark-matter halos (as approximated by R_{200}) of these H I-rich galaxies as circles in the top panel of Figure 4 and highlight them as red dots in the middle panel. Given that CGM absorbers are commonly found within $\pm 100\,{\rm km\,s^{-1}}$ of the host galaxies' systemic velocities (e.g., Werk et al. 2013), if these H I-rich LG galaxies contain CGM gas in their dark-matter halos, the CGM absorbers would be located at similar locations to the host galaxies on the position–velocity diagram. Indeed, as we show in the bottom panel of Figure 4, absorbers detected near IC 1613 (this work) are found to be mostly aligned with the H I from the Magellanic System, so do a large fraction of ion absorbers detected near M31 (Lehner et al. 2020).

We estimate the surface area of the CGM of each gas-rich galaxy with $A = 2\pi(1 - \cos\theta)(180/\pi)^2$ deg^2, where θ is the projected CGM radius in radians. The total surface area of the CGM of these galaxies is $\sim$3500 deg^2 if assuming 100% detection rate within R_{200}. In particular, the CGM of M31 accounts for nearly half of the total surface area ($\sim$1500 deg^2). Here we have taken into account the overlap of the CGM cross sections of adjacent galaxies. Given that the detection rate of CGM absorbers in low-mass galaxies is found to be significantly reduced beyond $0.5R_{200}$ (Bordoloi et al. 2014), if we only consider the CGM detection within $0.5R_{200}$ for the gas-rich galaxies in our sample but include the full CGM size of M31, the total surface area is $\sim$2000 deg^2. Our estimate shows that the cross sections of the extended CGM of LG gas-rich galaxies occupy a nonnegligible fraction of the sky near the Magellanic System in projection. Therefore, when considering the ionized cross section of the Magellanic system, one should take into account the contamination of potential CGM absorbers from distant gas-rich galaxies in the LG.

Though it is beyond the scope of this work to further investigate the true ionized extent of the Magellanic System or the origins of the ion absorbers, the overall ionized gas and dwarf galaxy environment in the Milky Way as well as in the LG should be examined closely in the future. We attempted to differentiate the Magellanic ionized gas from other sources using measurements such as detection rates, ion line ratios, and velocities in other rest frames (e.g., $v_{\rm GSR}$, $v_{\rm LGSR}$). None of the attempts led to conclusive answers on the actual extension of the Magellanic ionized gas. The similar kinematics of the Magellanic H I, Fox14's ion absorbers, and the LG dwarf galaxies indicates that the coincidence may be partially subject to the corotation of the solar system with the Milky Way. In fact, Richter et al. (2017) have also noted this coincidental alignment between the LG galaxies and ionized HVCs' absorption velocities. More investigation is needed to further understand the underlying physics of the coincidental alignments among different component in the LG.

ORCID iDs

Yong Zheng https://orcid.org/0000-0003-4158-5116
Andrew Emerick https://orcid.org/0000-0003-2807-328X
Mary E. Putman https://orcid.org/0000-0002-1129-1873
Jessica K. Werk https://orcid.org/0000-0002-0355-0134
Evan N. Kirby https://orcid.org/0000-0001-6196-5162
Joshua Peek https://orcid.org/0000-0003-4797-7030

References

Andrews, B. H., & Martini, P. 2013, ApJ, 765, 140
Asplund, M., Grevesse, N., Sauval, A. J., & Scott, P. 2009, ARA&A, 47, 481
Barger, K. A., Madsen, G. J., Fox, A. J., et al. 2017, ApJ, 851, 110
Bernard, E. J., Monelli, M., Gallart, C., et al. 2010, ApJ, 712, 1259
Bordoloi, R., Tumlinson, J., Werk, J. K., et al. 2014, ApJ, 796, 136
Bouché, N., Lehnert, M. D., Aguirre, A., Péroux, C., & Bergeron, J. 2007, MNRAS, 378, 525
Bowen, D. V., Tolstoy, E., Ferrara, A., Blades, J. C., & Brinks, E. 1997, ApJ, 478, 530
Bresolin, F., Urbaneja, M. A., Gieren, W., Pietrzyński, G., & Kudritzki, R.-P. 2007, ApJ, 671, 2028
Brooks, A. M., Governato, F., Booth, C. M., et al. 2007, ApJL, 655, L17
Bryan, G. L., & Norman, M. L. 1998, ApJ, 495, 80
Calura, F., Pipino, A., Chiappini, C., Matteucci, F., & Maiolino, R. 2009, A&A, 504, 373
Chabrier, G. 2003, PASP, 115, 763
Chisholm, J., Tremonti, C. A., Leitherer, C., Chen, Y., & Wofford, A. 2016, MNRAS, 457, 3133
Christensen, C. R., Davé, R., Brooks, A., Quinn, T., & Shen, S. 2018, ApJ, 867, 142
Christensen, C. R., Davé, R., Governato, F., et al. 2016, ApJ, 824, 57
Cole, A. A., Tolstoy, E., Gallagher, J. S. I., et al. 1999, AJ, 118, 1657
Dalcanton, J. J., Williams, B. F., Lang, D., et al. 2012, ApJS, 200, 18
Danforth, C. W., Keeney, B. A., Stocke, J. T., Shull, J. M., & Yao, Y. 2010, ApJ, 720, 976
D'Onghia, E., & Fox, A. J. 2016, ARA&A, 54, 363
El-Badry, K., Bradford, J., Quataert, E., et al. 2018, MNRAS, 477, 1536
Emerick, A., Bryan, G. L., Mac Low, M.-M., et al. 2018, ApJ, 869, 94
Ferland, G. J., Chatzikos, M., Guzmán, F., et al. 2017, RMxAA, 53, 385
Fox, A. J., Frazer, E. M., Bland-Hawthorn, J., et al. 2020, ApJ, 897, 23
Fox, A. J., Wakker, B. P., Barger, K. A., et al. 2014, ApJ, 787, 147
Gallazzi, A., Charlot, S., Brinchmann, J., White, S. D. M., & Tremonti, C. A. 2005, MNRAS, 362, 41
Garrison-Kimmel, S., Boylan-Kolchin, M., Bullock, J. S., & Lee, K. 2014, MNRAS, 438, 2578
Garrison-Kimmel, S., Bullock, J. S., Boylan-Kolchin, M., & Bardwell, E. 2017, MNRAS, 464, 3108
Gehrels, N. 1986, ApJ, 303, 336
Gil de Paz, A., Boissier, S., Madore, B. F., et al. 2007, ApJS, 173, 185
Giovanelli, R., Haynes, M. P., Adams, E. A. K., et al. 2013, AJ, 146, 15
Grcevich, J., & Putman, M. E. 2009, ApJ, 696, 385
Haardt, F., & Madau, P. 2001, in XXIst Moriond Astrophysics Meeting, Clusters of Galaxies and the High Redshift Universe Observed in X-rays, ed. D. M. Neumann & J. T. V. Tran (Paris: CEA), 64
Hafen, Z., Faucher-Giguère, C.-A., Anglés-Alcázar, D., et al. 2019, MNRAS, 488, 1248
Haffner, L. M., Reynolds, R. J., Tufte, S. L., et al. 2003, ApJS, 149, 405
Harris, C. R., Millman, K. J., van der Walt, S. J., et al. 2020, Natur, 585, 357
HI4PI Collaboration, Ben Bekhti, N., Flöer, L., et al. 2016, A&A, 594, A116
Howk, J. C., Wotta, C. B., Berg, M. A., et al. 2017, ApJ, 846, 141
Hunter, D. A., & Elmegreen, B. G. 2004, AJ, 128, 2170
Hunter, D. A., Ficut-Vicas, D., Ashley, T., et al. 2012, AJ, 144, 134
Hunter, J. D. 2007, CSE, 9, 90

Johnson, S. D., Chen, H.-W., Mulchaey, J. S., Schaye, J., & Straka, L. A. 2017, ApJL, 850, L10
Keeney, B. A., Danforth, C. W., Stocke, J. T., France, K., & Green, J. C. 2012, PASP, 124, 830
Kirby, E. N., Cohen, J. G., Guhathakurta, P., et al. 2013, ApJ, 779, 102
Kirby, E. N., Martin, C. L., & Finlator, K. 2011, ApJL, 742, L25
Kroupa, P. 2001, MNRAS, 322, 231
Lake, G., & Skillman, E. D. 1989, AJ, 98, 1274
Lee, H., Skillman, E. D., Cannon, J. M., et al. 2006, ApJ, 647, 970
Lehner, N., Berek, S. C., Howk, J. C., et al. 2020, ApJ, 900, 9
Liang, C. J., & Chen, H.-W. 2014, MNRAS, 445, 2061
Lucchini, S., D'Onghia, E., Fox, A. J., et al. 2020, Natur, 585, 203
Ma, X., Hopkins, P. F., Faucher-Giguère, C.-A., et al. 2016, MNRAS, 456, 2140
Mac Low, M.-M., & Ferrara, A. 1999, ApJ, 513, 142
Madau, P., & Dickinson, M. 2014, ARA&A, 52, 415
Markwardt, C. B. 2009, in ASP Conf. Ser. 411, Astronomical Data Analysis Software and Systems XVIII, ed. D. A. Bohlender, D. Durand, & P. Dowler (San Francisco, CA: ASP), 251, arXiv:0902.2850
Mathewson, D. S., Cleary, M. N., & Murray, J. D. 1974, ApJ, 190, 291
McConnachie, A. W. 2012, AJ, 144, 4
McQuinn, K. B. W., Skillman, E. D., Dolphin, A., et al. 2015a, ApJL, 815, L17
McQuinn, K. B. W., Skillman, E. D., Dolphin, A., et al. 2015b, ApJ, 812, 158
McQuinn, K. B. W., van Zee, L., & Skillman, E. D. 2019, ApJ, 886, 74
Moster, B. P., Somerville, R. S., Maulbetsch, C., et al. 2010, ApJ, 710, 903
Muratov, A. L., Kereš, D., Faucher-Giguère, C.-A., et al. 2017, MNRAS, 468, 4170
Nidever, D. L., Majewski, S. R., & Butler Burton, W. 2008, ApJ, 679, 432
Nidever, D. L., Majewski, S. R., Butler Burton, W., & Nigra, L. 2010, ApJ, 723, 1618
Patel, E., Kallivayalil, N., Garavito-Camargo, N., et al. 2020, ApJ, 893, 121
Peek, J. E. G., Babler, B. L., Zheng, Y., et al. 2018, ApJS, 234, 2
Peek, J. E. G., Heiles, C., Douglas, K. A., et al. 2011, ApJS, 194, 20
Peeples, M. S., Werk, J. K., Tumlinson, J., et al. 2014, ApJ, 786, 54
Price-Whelan, A., Sipocz, B., Major, S., & Oh, S. 2017, adrn/gala: v0.2.1, Zenodo, doi:10.5281/zenodo.833339
Putman, M. E., Gibson, B. K., Staveley-Smith, L., et al. 1998, Natur, 394, 752
Putman, M. E., Peek, J. E. G., & Joung, M. R. 2012, ARA&A, 50, 491
Putman, M. E., Staveley-Smith, L., Freeman, K. C., Gibson, B. K., & Barnes, D. G. 2003, ApJ, 586, 170
Rey, M. P., Pontzen, A., Agertz, O., et al. 2020, MNRAS, 497, 1508
Richter, P., Nuza, S. E., Fox, A. J., et al. 2017, A&A, 607, A48
Ritter, C., Côté, B., Herwig, F., Navarro, J. F., & Fryer, C. L. 2018a, ApJS, 237, 42
Ritter, C., Herwig, F., Jones, S., et al. 2018b, MNRAS, 480, 538
Romano, D., Calura, F., D'Ercole, A., & Few, C. G. 2019, A&A, 630, A140
Rubin, K. H. R., Prochaska, J. X., Koo, D. C., et al. 2014, ApJ, 794, 156
Rubin, K. H. R., Prochaska, J. X., Koo, D. C., & Phillips, A. C. 2012, ApJL, 747, L26
Salpeter, E. E. 1955, ApJ, 121, 161
Savage, B. D., & Sembach, K. R. 1991, ApJ, 379, 245
Savage, B. D., & Sembach, K. R. 1996, ARA&A, 34, 279
Silich, S., Lozinskaya, T., Moiseev, A., et al. 2006, A&A, 448, 123
Skillman, E. D., Hidalgo, S. L., Weisz, D. R., et al. 2014, ApJ, 786, 44
Skillman, E. D., Tolstoy, E., Cole, A. A., et al. 2003, ApJ, 596, 253
Stocke, J. T., Keeney, B. A., Danforth, C. W., et al. 2013, ApJ, 763, 148
Telford, O. G., Werk, J. K., Dalcanton, J. J., & Williams, B. F. 2019, ApJ, 877, 120
The Astropy Collaboration, Price-Whelan, A. M., Sipőcz, B. M., et al. 2018, AJ, 156, 123
Tremonti, C. A., Heckman, T. M., Kauffmann, G., et al. 2004, ApJ, 613, 898
Tumlinson, J., Thom, C., Werk, J. K., et al. 2013, ApJ, 777, 59
Vogelsberger, M., Zavala, J., Simpson, C., & Jenkins, A. 2014, MNRAS, 444, 3684
Wakker, B. P., Hernandez, A. K., French, D. M., et al. 2015, ApJ, 814, 40
Weisz, D. R., Dolphin, A. E., Skillman, E. D., et al. 2014, ApJ, 789, 147
Werk, J. K., Prochaska, J. X., Thom, C., et al. 2013, ApJS, 204, 17
Werk, J. K., Prochaska, J. X., Tumlinson, J., et al. 2014, ApJ, 792, 8
Zheng, Y., Peek, J. E. G., Putman, M. E., & Werk, J. K. 2019a, ApJ, 871, 35
Zheng, Y., Peek, J. E. G., Werk, J. K., & Putman, M. E. 2017, ApJ, 834, 179
Zheng, Y., Putman, M. E., Emerick, A., et al. 2019b, MNRAS, 490, 467